



An in-depth observational and modeling analysis to explore long-range offshore wakes under different stability regimes

Elizabeth J. McCabe¹, Jeffrey M. Freedman¹, Philippe Beaucage², Nick Robinson², Akila Gothandarman²

¹Atmospheric Sciences Research Center, University at Albany, State University of New York, Albany, NY 12226, USA

5 ²UL Solutions

Correspondence to: Elizabeth McCabe (emccabe@albany.com)

Abstract. As wind energy areas continue to be built out worldwide, it is increasingly important to understand the implications of long-range wind farm wakes on wind energy generation. While gross capacity factors can be estimated, the impacts of upstream wind farm wakes on downstream energy production, especially under stable conditions, are largely unknown. A clear understanding of marine atmospheric boundary layer (MABL) stability in offshore regions is still evolving, as continuous high-resolution thermodynamic profiles in the MABL are uncommon. Given the relationship between stability and long-range (> 50 km) offshore wakes, it is increasingly important to reliably estimate stability conditions in offshore regions. With the lack of consistent observations in and around offshore wind farms, it is necessary to rely on mesoscale models such as the Weather Research and Forecasting (WRF) modeling system to estimate stability and wake lengths. For this work we test WRF's ability to reproduce wake effects and potential losses using flight data over wind farms in North Sea to evaluate its performance. As thermal stability is critical to understanding wake length, different metrics are evaluated to determine the best way to parameterize atmospheric stability from the WRF model. Results show that the bulk Richardson number derived from WRF can be used as a reliable metric to classify stability and that wake lengths are well represented under stable conditions.

1 Introduction

20 It is widely accepted that offshore wind farm wakes can propagate downstream beyond 50 km under stable atmospheric conditions (Fitch et al. 2012; Platis et al. 2018; Cañadillas et al. 2020; Golbazi et al. 2022; Ali et al. 2023; Hahmann et al. 2025). While downwind wakes from turbines facilities onshore have been extensively studied (Lundquist et al. 2019; Debnath et al. 2022; NREL 2022; Krishnamurthy et al. 2024; Rogers 2024), wind farm waking in the offshore meteorological-oceanographic (“met-ocean”) environment remains less understood. Understanding the frequency, extent, and deficits in wakes, and their relationship to offshore atmospheric stability, will help improve resource and energy yield assessment as well as wind farm production forecasting.

25 Wind farm wakes are a product of momentum sinks and turbulent kinetic energy (TKE) generation from large turbine arrays (Fitch et al. 2012; Golbazi et al. 2022; Hahmann et al. 2025) resulting in a downwind speed reduction and an increase in turbulence. Previous modeling studies performed over the United States East Coast have found a wind speed deficit, on



30 average, of 2 m s^{-1} within a simulated wind farm and 0.5 m s^{-1} in the downwind wake (Golbazi et al. 2022). Although
offshore wakes have been found to generally extend about 50 km downwind, very stable conditions may result in even
longer wakes, potentially reaching distances of 100 km (Fitch et al. 2012; Platis et al. 2018; Cañadillas et al. 2020; Golbazi
et al. 2022; Ali et al. 2023; Hahmann et al. 2025). These wakes can be further amplified by wind direction based on the
upwind fetch or wind direction alignment with the wind farm turbine rows (Platis et al. 2020; Hahmann et al. 2025).

35 Over land, wakes are generally shorter in distance as a higher surface roughness and more ambient turbulence allows
them to dissipate more quickly (Platis et al. 2018; Pryor 2024). However, the ocean often features lesser turbulence due to a
smoother surface and reduced thermal convection (Barthelmie 1999; Hansen et al. 2012; Platis et al. 2018; Pryor et al. 2024).
A yearlong study in the offshore waters of Denmark (Barthelmie 1999) found stable and near neutral conditions occur 36%
and 53% of the time, compared to only 11% for unstable cases (Hahmann et al. 2025).

40 A major limitation to understanding how wind farm wakes behave offshore is a lack of measurements in areas within and
directly downwind of wind farms. The North Sea offers a long duration of offshore wind deployment, beginning in 2001
with construction of the first modern large-scale (160 MW) wind farm, Horns Rev 1 (Ørsted 2019; Kihlström 2023;
Vattenfall 2025). In-situ measurements in the region include meteorological towers, Forschungsplattformen in Nordund
Ostsee (FINO) 1 and 3, which were un-waked prior to 2010 and 2014, respectively, but are now located within and alongside
45 turbine arrays.

As a result of limited in-situ measurements of offshore wakes, research of the downwind wake generally relies on SAR
satellite imagery (Christiansen and Hasager 2005, 2006; Hasager 2015; Djath et al. 2018, 2022) or operational turbine
SCADA data (Foreman et al. 2024). However, two flight campaigns in the late 2010s provided some of the first
measurements of offshore wind farm downwind wakes. The WInd Park Far Field (WIPAFF) campaign in 2016 and 2017
50 included a total of 41 research flights (Platis et al. 2018) and X-Wakes collected data from an additional 49 flights in 2020
and 2021 (Rausch et al. 2023). Previous analysis on the WIPAFF measurements by Cañadillas et al. (2020) and Berge et al.
(2024) note a phase error when comparing these observations to mesoscale models, given that each flight occurs over a
period of a few hours.

Current engineering wake models used in the wind industry, such as the DAWM-EV (Brower and Robinson 2009) and
55 TurbOPark (Nygaard et al. 2020; Pedersen et al. 2022), perform well at simulating internal wake losses, however, they do
not include different atmospheric stability classes, thus they show faster wake recovery than is observed and are not able to
capture wind speed deficits at downstream distances of 40-50 km (Fischereit et al. 2021; Stoelinga et al. 2022; Fischereit et
al. 2022; Berge et al. 2024; Porchetta et al. 2024). Higher fidelity modeling is necessary to capture long-range wakes under
non-neutral thermal conditions; however, large eddy simulations (LES) are computationally expensive when simulating large
60 wind farms (Xia et al. 2017; Zhan et al. 2020). Therefore, recent studies have been relying on mesoscale numerical weather
prediction (NWP) models such as the Weather Research and Forecasting (WRF) modeling system that are more practical for
modeling large wind farms at regional scales (Xia et al. 2017; Fischereit et al. 2021; Stoelinga et al. 2022).



Long-range wakes can be modeled in the WRF model version 3.3 or later with the inclusion of the Fitch parameterization (Fitch et al. 2012; Archer et al. 2020; Skamarock et al. 2021) or the Ma–Archer–Vasel–Be–Hagh (MAV) scheme (new in WRF version 4.6.0; Ma et al. 2022). The limited availability of long-term data useful for analyzing offshore wind farm wakes necessitates reliance on atmospheric models with a full physics parameterization suite, such as WRF, to understand the offshore wind resource and variability and to predict wake losses (McCabe and Freedman 2025). However, very few studies have been able to validate the accuracy of the WRF model for capturing wake losses, wake extent, and the relationship to stability in an offshore environment. Berge et al. (2024) was among the first to compare the data from the WIPAFF flights using WRF simulations, modeling 4 of the 41 flights. They found that WRF performed well in capturing wake losses, especially in proximity (20–30 km) of the farms. In this study, 41 flight cases from the WIPAFF experiment and long-term measurements at the FINO3 tower in the North Sea are used to validate WRFs ability to predict thermal stability and accurately simulate long-range (> 50 km) offshore wakes.

This paper is organized as follows: Data used to validate the WRF model is described in Sect. 2. Methods used in the analysis are discussed in Sect. 3. Section 4 uses the results from the WIPAFF flight experiments to compare against the WRF model. Section 5 uses the results of the model validation to better understand the meteorological environment in the North Sea. Summary and conclusions are discussed in Sect. 6.

2 Data

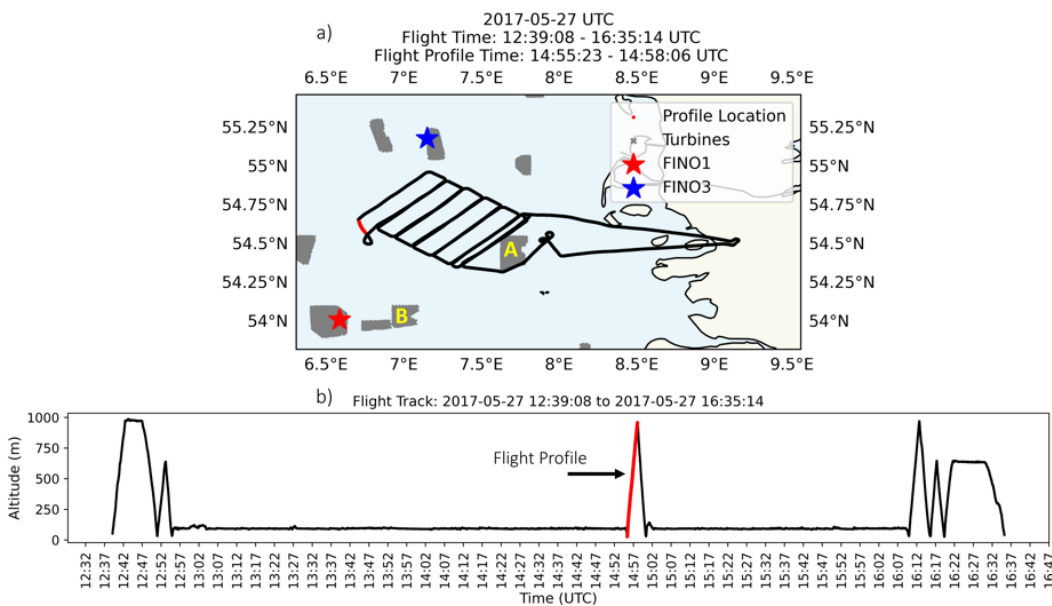
2.1 WIPAFF Flights

The WIPAFF campaign features the first offshore *in situ* measurements of the region downwind of large wind farms (Platis et al. 2018). In 2016 and 2017 a Dornier DO 128 research aircraft flew 41 flights over wind farms in the German Bight (specifically focusing on wind farm grouping Amrumbank West, Nordsee Ost and Meerwind Süd/Ost, as well as Gode Wind 1 and 2; Fig. 1a). Measurements used here include the aircraft's position (coordinates, altitude, aircraft velocity, roll, pitch, and heading using a combination of an inertial measurement unit [IMU] and GPS), wind speed and direction (estimated from the u , v , and w components), air temperature, relative humidity, density, and pressure at 100 Hz (Platis et al. 2018). Instruments used include a Rosemount 5-Hole-Probe (for wind components), Rosemount 1221 and 1201 pressure transducers, Rosemount temperature sensor (fast and slow), and a Meteolabor Dew Point Mirror (humidity; Corsmeier et al. 2001; Platis et al. 2018). Measurements of sea surface temperature were recorded through a LiDAR scanning system (Platis et al. 2018). Details on other instruments on the aircraft can be found in Corsmeier et al. (2001). Flights lasted 2–4 hours, with the downwind flight pattern generally shorter (~1 hour; Platis et al. 2018). Aircraft speed was 66 m s^{-1} and the flight tracks were flown at hub height (approximately 95 or 120 m depending on wind farm cluster) perpendicular to the mean wind direction, up to 50 km directly downwind of the wind farm (Fig. 1). Of the 41 flights, only 25 cases measure the wake directly downstream of the turbine (such as shown in Fig. 1a); the other 16 flights flew above the turbine rotor plane. Data were collected at a sampling rate of

100 Hz, and averaged to 15 sec (approximately every 1 km, chosen to match the 1 km spatial resolution in the WRF model output) for the purpose of this study.

In addition to the horizontal flight legs, the aircraft also measured atmospheric profiles through a steep ascent from approximately 50 m to 1000 m AMSL (Fig. 1b; Platis et al. 2018). These profiles are averaged to 1 sec, providing measurements at vertical height intervals ranging from 2 to 12 meters. All flight profiles are taken outside of the waked region, so they are not directly impacted by wind farms (Fig. 1).

100



105 **Figure 1:** a) Flight plan on 27 May 2017 showing an entire flight track from take off to landing. Blue and red stars indicate the location of the FINO towers. Wind farms are represented by areas shaded in grey. Wind farm clusters composed of Amrumbank West, Nordsee Ost and Meerwind Süd/Ost are shown by the letter A, and Gode Wind 1 and 2 by the letter B. b) Timeseries of flight altitude (m) across entire flight track, with the red line showing the location of the atmospheric profile chosen for this flight.

2.2 FINO Towers

In-situ offshore measurements have been collected at FINO1 since 2003, FINO2 since 2007, and FINO3 since 2009. Towers FINO1 and FINO3 are in the North Sea in proximity to the location of the WIPAFF flight campaign (Figs 1a and 2). FINO2 is located further east in the Baltic Sea and is not relevant to this study. For brevity, results focus on FINO3 (55° 11,7 'N, 007° 110 9,5' E). While FINO3 has been operational since 2009, after 2013 the tower was surrounded by operational wind farms (Sandbank and Dan Tysk). FINO3 measurements used include air temperature (at 29 m and 95 m ASL), relative humidity (29 m and 95 m), pressure (23 m and 95 m), and wind speed and direction (51 m, 71 m, and 91 m). The power law equation (see Eq. 1) is used to estimate wind speeds at 29 m AMSL from calculated wind speed shear between measurement heights 51 m and 71 m AMSL (Eq. 2).



$$115 \quad \bar{U} = \bar{U}_r \left(\frac{z}{z_r}\right)^\alpha \quad (1)$$

$$\alpha = \frac{\ln(\bar{U}/\bar{U}_r)}{\ln(z/z_r)} \quad (2)$$

Where α is the vertical speed shear, \bar{U} is the wind speed (m s^{-1}), z is the height (m), and \bar{U}_r is the wind speed at a reference height, z_r .

120 3 Methods

3.1 WRF Model Setup

WRF model version 4.6.1 is used to conduct 36-hour simulations, including a 12-hour spin-up. The 27 simulations were centered over the North Sea region (Fig 2; see days that were simulated in Table 4). The WRF model is initialized using ERA5, the fifth generation ECMWF atmospheric reanalysis (ECMWF 2019; Hersbach 2020) and a one-way nested 3-domain setup, with grid resolutions of 9 km, 3 km, and 1 km (Table 1). Wind farms are included in the model using the Fitch Wind Farm Parameterization (WFP; Fitch et al. 2012; Archer et al. 2020). The Fitch WFP is compatible with the MYNN2 (Nakanishi and Niino 2006; Nakanishi and Niino 2009; Olson et al. 2019) PBL parameterization with corrections suggested by Archer et al. (2020) incorporated into WRF model version 4.2.1 *et seq.* These corrections included a bug fix and a reduction of added turbulence kinetic energy (TKE) to be a quarter of the original value (Archer et al. 2020). Other model physics choices are shown in Table 1.

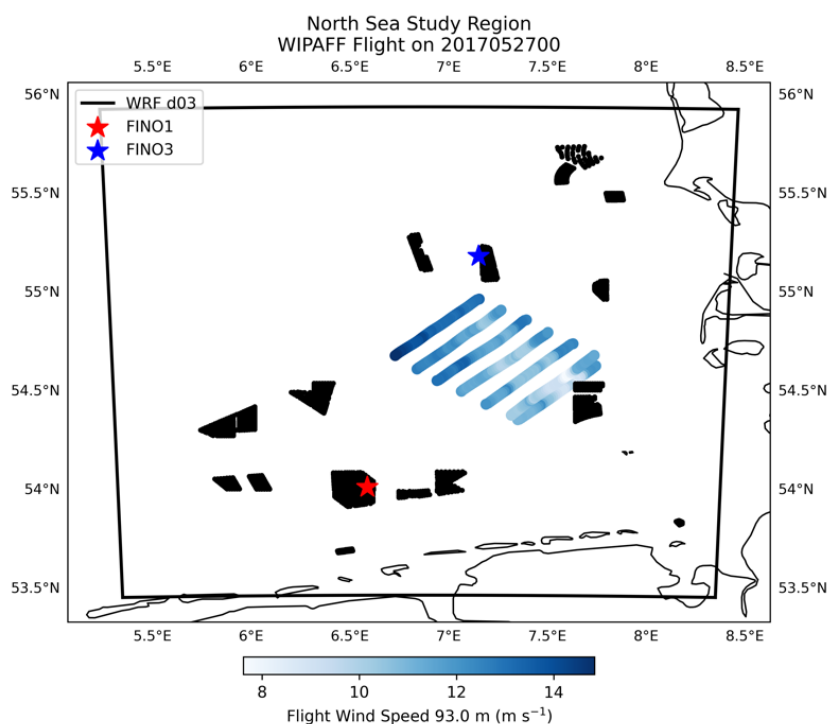
Table 1. Model setup used for WRF experiments

WRF model v4.6.1			
	D01	D02	D03
Initial and lateral boundary conditions	ERA5		
Grid spacing (km)	9 km	3 km	1 km
Cumulus scheme	Kain-Fritsch	None	None
Vertical Levels	40 (16 below 1000 m)		
Microphysics	WRF Single-Moment 5-class scheme WSM5		
Longwave/Shortwave radiation	RRTM		
Planetary boundary layer physics	MYNN2 (Nakanishi and Niino 2006; Nakanishi and Niino 2009; Olson et al. 2019)		
Surface layer physics	MYNN		



Land surface physics	Noah Land Surface Model
Wind Farm Parameterization	Fitch

135 Model simulations are performed over German Bight region of the North Sea, and analysis focuses on the innermost domain (D03; Fig 2). Hub heights over the North Sea are 85–110m AMSL, and turbines rated capacity ranges from 2 to 9 MW depending on the array. Turbine placement is set as the wind farms are already operational (Fig 2; Nick Robinson, personal communication, October 2024). Both operational and planned wind farms outside of the inner domain region are not considered in this analysis.



140 **Figure 2: WRF (version 4.6.1) inner domain (d03) extent over the North Sea. FINO towers 1 and 3 are shown by the red and blue stars. Location and wind speed (ms^{-1}) of the WIPAFF flight on 27 May 2017 is also shown. Wind turbines used in the simulations are represented black scatter points.**

3.2 Stability Calculations

145 Different methods for estimating atmospheric stability from the WRF model are evaluated for the analysis. While the Monin-Obukhov stability parameter (defined as the ratio of height $[z]$ to the Obukhov length $[L]$) is frequently used to classify stability (Monin and Obukhov 1954; Barthelmie 1999; Floors et al. 2011; Archer et al. 2016; Cantero et al. 2022; Rosencrans et al. 2024), in this study, L cannot be derived from available observations as there are no available *in situ* flux measurements. We



therefore consider stability metrics that allow for direct comparison between the stability derived from WRF and observations.

150 These include:

1. The **Bulk Richardson number** (Ri_b), an approximation of the Gradient Richardson number, which estimates stability using local gradients of wind and virtual potential temperature (Eq. 3; Stull 1988). The Ri_b considers turbulence generated both mechanically and buoyantly and is given by

$$Ri_b = \frac{g \Delta \overline{\theta}_v \Delta z}{\overline{\theta}_v [(\Delta \overline{U})^2 + (\Delta \overline{V})^2]} \quad (3)$$

155 where Δz represents the thickness (m) of the layer, $\overline{\theta}_v$ is the mean layer virtual potential temperature (K), and U and V represent the gradient in the wind components of the layer ($\text{ms}^{-1}\text{m}^{-1}$). As Ri_b (further referred to as the "Bulk Ri Formulation"), is an approximation, there are no universally established thresholds that define when the flow changes from stable to unstable (Stull 1988). Mohan and Siddiqui (1998) use 7 stability classes for Ri_b , and has been used in recent studies (Olsen et al. 2017; Ruisi and Bossanyi 2019). This compares with more simple classification schemes,
 160 such as the 3-class scheme used in Pronk et al. 2022. Their Bulk Ri Formulation (see Table 2) is based on 188 hours of data collected from a tall tower in a rural location located in central Illinois (USA; Mohan and Siddiqui 1998). Given that the performance of the Bulk Ri Formulation is poor when comparing observations to model output (see further discussion below), the Businger and Businger-Hicks formulation laid out in Mohan and Siddiqui (1998) are also considered (Table 2)

165

Table 2. Summary of Ri_b stability classifications.

Stability Class	Ri_b			
	Mohan and Siddiqui 1998			Pronk et al. 2022
	<i>Businger-Hicks Formulation</i>	<i>Businger Formulation</i>	<i>Bulk Ri Formulation</i>	<i>3-Class Simplification</i>
Very Unstable	$Ri_b < -5.34$	$Ri_b < -2.038$	$Ri_b < -0.023$	$Ri_b < -0.025$
Unstable	$-5.34 \leq Ri_b < -2.26$	$-2.038 \leq Ri_b < -0.75$	$-0.023 \leq Ri_b < -0.011$	
Weakly Unstable	$-2.26 \leq Ri_b < -0.569$	$-0.75 \leq Ri_b < -0.18$	$-0.011 \leq Ri_b < -0.0036$	
Neutral	$-0.569 \leq Ri_b < 0.083$	$-0.18 \leq Ri_b < 0.083$	$-0.0036 \leq Ri_b < 0.0072$	$-0.025 \leq Ri_b \leq 0.025$
Weakly Stable	$0.083 \leq Ri_b < 0.196$	$0.083 \leq Ri_b < 0.16$	$0.0072 \leq Ri_b < 0.042$	$Ri_b > 0.025$
Stable	$0.196 \leq Ri_b < 0.49$	$0.16 \leq Ri_b < 0.18$	$0.042 \leq Ri_b < 0.084$	
Very Stable	$Ri_b \geq 0.49$	$Ri_b \geq 0.18$	$Ri_b \geq 0.084$	

170 2. The gradient of θ_v , or **lapse rate** δ , is a simpler way to assess stability, as it only considers the change in θ_v over a specified layer. Note, that the thickness of this layer (values for Δz) varies based on observational data heights available.



$$\delta = \frac{\Delta\theta_v}{\Delta z} \quad (4)$$

Where Δz represents the thickness (m) of the layer and $\Delta\theta_v$ is the difference in θ_v (K) across the layer. This is a simple approximation for stability, and while it is generally assumed that negative values are unstable and positive values are stable, for the purpose of this study values of less than or equal to -0.01 K m^{-1} are unstable, greater than or equal to 0.01 K m^{-1} are stable, and anything between are neutral. This is a modification of the of the classes presented in Cañadillas et al. (2022) as the classes presented in that study were not sensitive enough to decipher between neutral and unstable/stable conditions.

3. The **air-sea temperature difference** ($\Delta T_{\text{Air-SST}}$) is the simplest approach, as it is often the most accessible approximation of atmospheric stability over water (it only requires surface measurements, which are generally more available in offshore regions). Generally, warm air over cold water indicates stable conditions, while cold air over warm water indicates unstable conditions. The $\Delta T_{\text{Air-SST}}$ is defined as the difference between the surface air temperature (here 2 m is used) and the SST. Stability classes are defined in Table 3.

Table 3. Stability classification thresholds for the $\Delta T_{\text{Air-SST}}$ (K).

Stability Class	$\Delta T_{\text{Air-SST}}$ $\Delta T = T_{2\text{m}} - T_{\text{SST}}$
Unstable	$\Delta T < -1.5$
Weakly Unstable	$-1.5 \leq \Delta T < -0.5$
Neutral	$-0.5 \leq \Delta T < 0.5$
Weakly Stable	$0.5 \leq \Delta T < 1.5$
Stable	$1.5 \leq \Delta T$

3.3 Capping Inversion Height

The capping inversion height (CIH) is defined as the height above the surface layer at which the potential temperature (θ) begins to increase, and a statically stable layer remains above, acting as the interface between the mixed layer and the free atmosphere (Stull 1988). To determine the CIH, the strongest discontinuity in θ and specific humidity (q) within the lowest 1000 m are identified (Ball 1960; Tennekes 1973; Deardorff 1979; Garstang and Fitzjarrald 1999; Rampanelli and Zardi 2004). Furthermore, the estimated inversion strength (EIS) is calculated using a method adapted from Wood and Bretheron (2006) and Wang et al. (2023).

To determine the CIH and EIS, the height of the strongest (positive) θ gradient is identified (Rampanelli and Zardi 2004). As validation, the location of the strongest (negative) gradient in the q is also identified, as at the top of the mixed layer an increase in θ and a corresponding decrease in q is observed (Stull 1988; Garstang and Fitzjarrald 1999; McCabe and Freedman 2025). To compare layers of equivalent thickness, all profiles, observed or modeled, are linearly interpolated to 30-m intervals.



Given the profile limitations of the flight (only extending up to approximately 1000 m AMSL) the maximum gradient (in flight and WRF output) must occur within the lowest 1000. This ensures consistency between how the WRF and flight profiles are compared.

200 Using the maximum gradient as the baseline height, the EIS is then calculated across 3 levels (Wood and Bretheron 2006; Wang et al. 2023):

1. Maximum gradient height and one level above
2. Maximum gradient height and two levels above
3. One level below maximum gradient height and one level above

205 The EIS is calculated between the 3 layers described above, using:

$$EIS = (\theta_{top} - \theta_{bottom}) - \Gamma_m(z_{top} - z_{bottom}) \quad (4)$$

where θ is the potential temperature at the top and bottom of the layer, and Γ_m is the moist adiabatic potential temperature gradient across the layer (Wang et al. 2023), given by

$$\Gamma_m = \left(\frac{1000}{p}\right)^{\frac{R_a}{c_{pa}}} \times \frac{g}{c_{pa}} \left(1 - \left(\frac{1+L_v q_s/R_a T}{1+L_v^2 q_s/c_{pa} R_v T^2}\right)\right) \quad (5)$$

210 where R_a is the specific gas constant and c_{pa} is the specific heat capacity for dry air at pressure (p), L_v is the latent heat and R_v is the specific gas constant for water vapor, and T is the air temperature. The moist adiabat is used as the inversion height is often close to saturation over the marine atmospheric boundary layer (MABL; Wang et al. 2023). Taking the largest value of the calculated EIS across the 3 layers, the CIH is determined to be the mean height of that layer (Wang et al. 2023). Note that, if the EIS is < 0.5 K, it is too weak to be considered an inversion and is disregarded, and the assumption is made that the CIH
215 does not occur within the limitations of the profile.

4 Part I: German Bight Model Validation

To validate the WRF model's ability to properly represent long-range wakes in an offshore environment, the WRF model's forecast of the wakes are compared to the 41 WIPAFF flight cases. The goal is to validate WRF's accuracy in capturing
220 downwind wakes and its ability to represent atmospheric stability. The study area focuses on the North Sea, specifically the German Bight region north and east of the German coast between approximately 5.5°-8.5° E and 53.5°-55.6° N (Fig. 2). Analysis time is presented in UTC, (1 hour behind local Central European Time (CET or 2 hours behind during summer, or CEST).

225 4.1 Flight Analysis

This is the first study to provide an in-depth observationally-based assessment of the ability of the WRF-WFP to represent offshore long-range wind farm wakes in the context of atmospheric stability. Using the WRF model to capture wind farm wakes is critical to reducing resource and forecast uncertainty given global development of offshore wind. However, one problem with directly comparing flight data to the WRF model is the differences in temporal and spatial scales. WRF provides



230 us with forecasts at a specific point in time (in this study, at 10-min intervals) with a spatial resolution of 1 km; however, the flights are taking point measurements at a frequency of 100 Hz over periods of a few hours (Fig. 1; Cañadillas et al. 2020; Berge et al. 2024).

Given the uncertainties in the spatial and temporal changes in wind speed that is inevitable with flight data, and the known timing phase error sometimes present in WRF (Cañadillas et al. 2022; Berge et al. 2024; McCabe and Freedman 2025), to determine the proper time offset when comparing the WRF analysis to observations, the wind speed prediction along the flight track is compared to the WRF model forecast along the same path (Fig. 3). By identifying the nearest latitude/longitude coordinate to the flight observations, the closest time to the nearest 10-min WRF output file and interpolating to the proper height (91 m AMSL on 6 September 2016 and 94 m AMSL on 27 May 2017), the modeled and observed windspeed are compared along the flight track (Figures 3, 4, and 5). Following the method described in Berge et al. (2024), the WRF forecasts for up to 3-hours prior and following the flight time is also considered to identify any time offsets. A time offset as large as +/- 5 hours was considered for all cases, but wind speed phase errors were found to occur within a threshold of 3 hours.

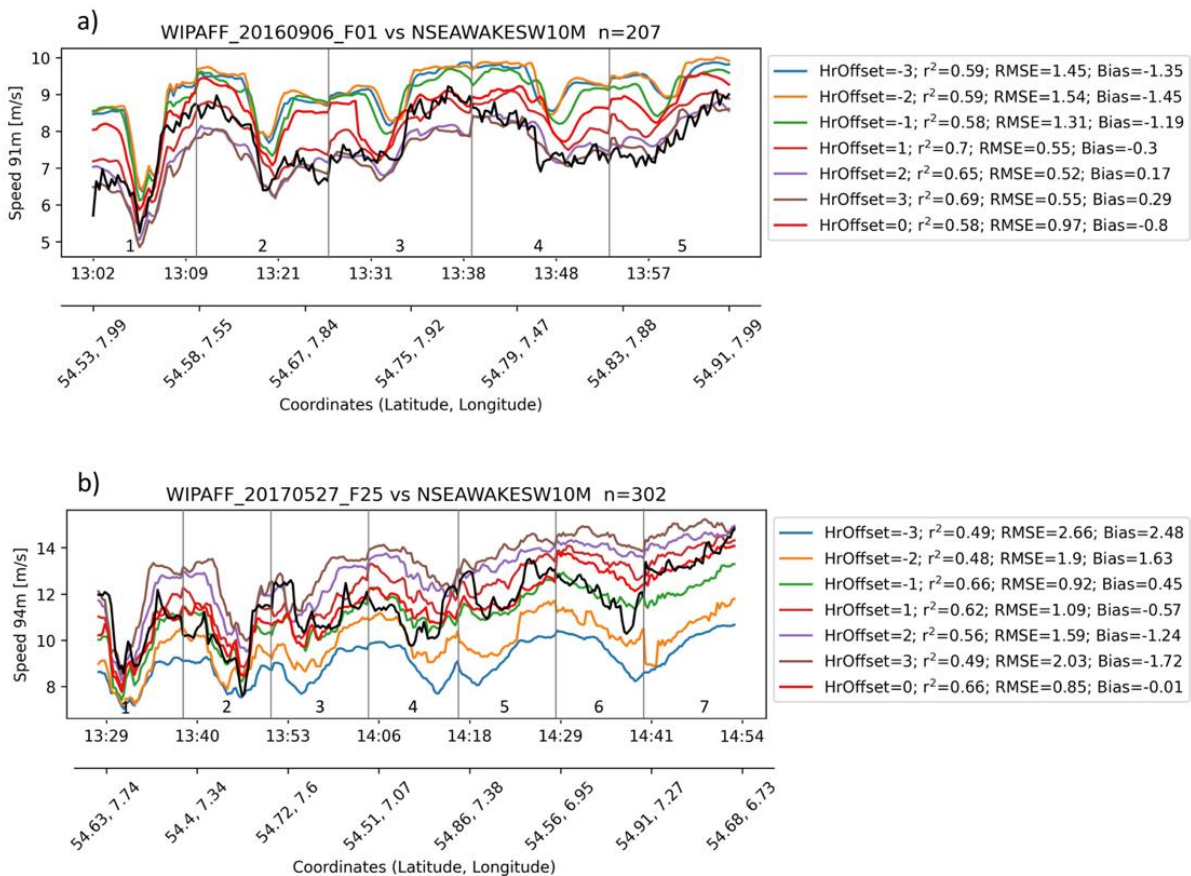
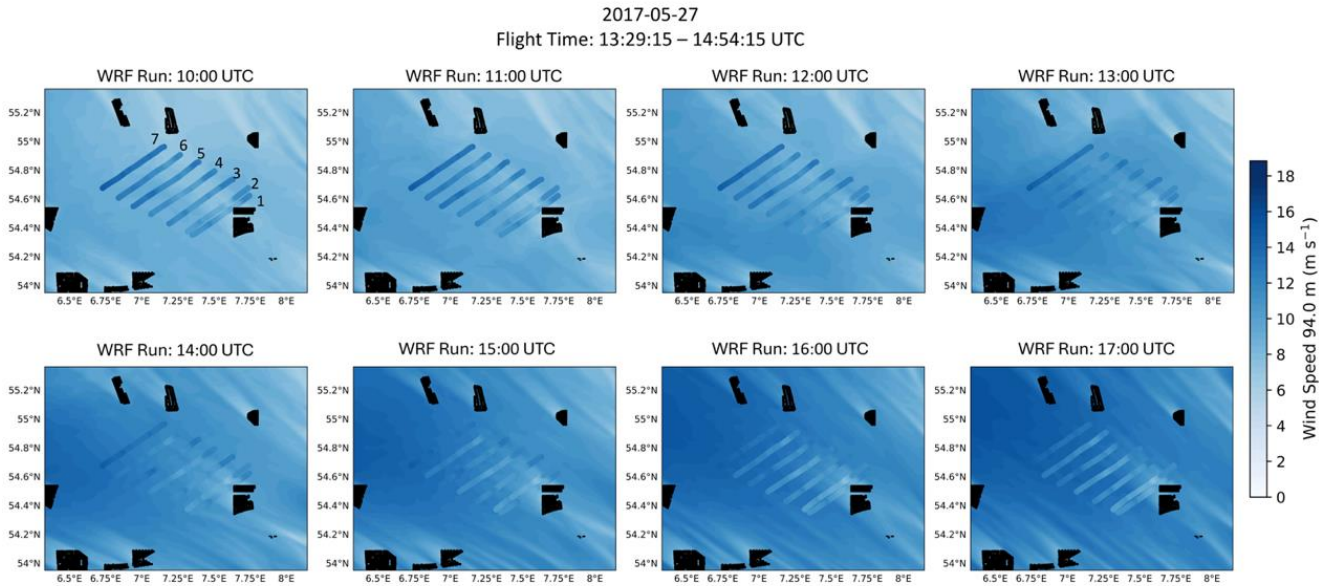




Figure 3: Wind speed (m s^{-1}) along horizontal flight legs (numbered and shown in Figs. 4 and 5). Observed wind speed (black) is compared to WRF wind speed for different time offsets (± 3 hours) for a) 6 September 2016 (see Fig. 5) and
245 **b) 27 May 2017 (See Fig. 4).**

To account for a phase error in the analysis, various WRF forecast hours are compared with the flight observations using metrics including the coefficient of determination (r^2), root mean square error (RMSE), and the mean bias error (MBE). The hour offset with the best combination of a high r^2 , low RMSE, and low MBE is determined to be the WRF phase error for that
250 case. While all three metrics do not always agree, the MBE and RMSE are weighted higher than the r^2 . This decision follows the discussion in McCabe and Freedman (2025), noting that r^2 has limitations in timeseries analysis to determining overall agreement between model results and observations. For example, the time offset used in the analyses for 27 May 2017 and 6 September 2016 is 0 and +2, respectively (Fig. 3 and Table 4).

To visualize the general performance of the WRF model in terms of the presence of a timing phase error, the flight-
255 measured windspeed is overlaid with the WRF-predicted wind field. For example, on 27 May 2017, the flight duration of the cross-wake horizontal legs (Fig. 3) spanned just under an hour and a half, from 13:29 UTC to 14:54 UTC. In addition to overlaying the WRF wind field for the hours concurrent with the flight (e.g., 13 and 14 UTC), the WRF wind speed prediction is again considered for the 3 hours before and after the flight time. This allows for a qualitative understanding of overall WRF model performance in capturing the wake and the wind field change over the duration of the flight. On 27 May 2017, WRF
260 performance is best in the hours coinciding with the flight, with a slight overprediction in the wind speed outside of the wake (Fig. 4). That said, WRF does well in representing the area of the largest wind speed deficit and the approximate length of the wake (Fig. 4).



265 **Figure 4: WRF wind field on 27 May 2017 (contours) overlaid with wind speed (m s^{-1}) measurements from WIPAFF flight (scatter points) for hours from 10:00 UTC to 17:00 UTC. Black shaded areas represent wind farm locations. Consecutive flight legs are numbered in the upper left panel.**

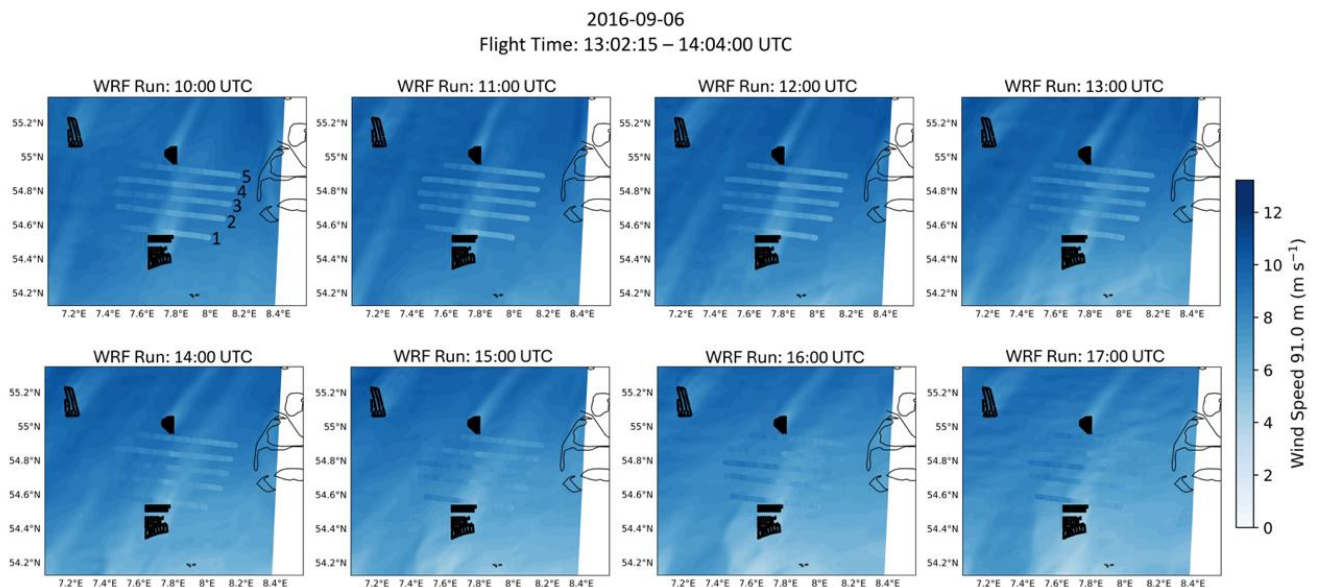


Figure 5: Same as Fig. 4, but for 6 September 2016.



For the 6 September 2016 flight WRF performs well in modeling the approximate length and region of the largest wind speed deficit. However, a time syncing problem is noted on 6 September 2016, as 16 and 17 UTC, the hours directly after those concurrent with the flight time, best represent the measured wind field (Figs. 3a and 5). This method was repeated for all 41 WIPAFF flights, and the WRF hour offsets used in the analysis for all cases are shown in Table 4.

275

Table 4: Columns (left to right) show the flight start time (UTC), the mean aircraft altitude (m) along the selected flight path, the determined WRF phase error (hours), stability metrics including the stability classification from the flight and WRF profile for each case, calculated using the Businger-Hicks Formulation. VS=Very Stable, S=Stable, WS=Weakly Stable, N=Neutral, WU=Weakly Unstable, U=Unstable, and VU=Very unstable. Ri_b bias (Flight– WRF) is also shown. Lastly, wind speed metrics including r^2 , RMSE, MBE, and n (number of points compared) are calculated between the flight and WRF along the flight track (such as shown in Fig. 3)

280

Flight Start Date/Time (UTC) Y/M/D HR	Mean Horizontal Leg Altitude (m)	WRF Phase Error (hrs)	Stability Metrics		Wind Speed Timeseries Metrics			
			Ri_b Stability Flight/WRF	Ri_b Bias Flight - WRF	r^2	RMSE	MBE	n
2016/09/06 12:13	91	2	WS/S	-0.27	0.65	0.52	0.17	207
2016/09/07 07:27	92	-3	VS/VS	-0.27	0.43	0.57	-0.19	135
2016/09/07 12:06	91	3	S/VS	-0.98	0.06	0.79	-0.23	110
2016/09/08 08:39	90	0	S/S	-0.02	0.55	0.48	0.14	226
2016/09/09 09:00	100	3	VS/N	1.4	0.08	0.83	0.06	430
2016/09/09 13:42	276	3	VS/N	2.29	0.28	0.58	-0.04	208
2016/09/10 07:43	93	-1	N/N	-0.09	0.69	0.93	-0.77	214
2016/09/10 12:17	90	0	N/N	-0.03	0.76	1.45	-1.42	134
2017/03/30 13:57	128	-3	S/S	0.04	0.03	1.66	0.84	227
2017/03/31 13:36	245	1	S/S	-0.04	0.88	3.22	2.09	35
2017/04/05 13:34	122	1	N/N	0.16	0.2	0.81	0.25	220
2017/04/06 13:29	183	0	WS/N	0.38	0.59	0.61	-0.05	136
2017/04/09 10:36	122	2	WS/VS	-1.16	0.54	1.19	0.76	261
2017/04/09 14:31	121	-2	VS/VS	-1.45	0.51	2.65	-2.22	86
2017/04/11 09:21	249	2	VS/N	0.64	0.01	0.81	-0.23	274
2017/04/11 14:07	121	0	N/N	-0.06	0.03	1.11	-0.04	164
2017/04/13 11:32	121	-3	N/N	0.03	0.13	1.15	0.6	146
2017/05/17 11:31	216	0	VS/VS	-1.09	0.87	0.94	0.64	64
2017/05/17 15:16	216	0	S/S	0.04	0.76	1.26	0.96	423
2017/05/23 07:34	124	-1	S/S	0.03	0.0	2.07	1.77	145
2017/05/23 11:18	247	3	N/N	0.13	0.01	1.06	0.14	169
2017/05/24 05:40	123	-2	N/N	0.09	0.64	1.31	-1.09	182
2017/05/24 10:13	245	-1	WS/VS	-0.54	0.12	1.17	-0.15	48
2017/05/27 08:45	95	1	N/VS	-0.64	0.49	1.08	0.52	282



2017/05/27 12:39	94	0	WS/S	-0.1	0.66	0.85	-0.01	302
2017/05/31 09:05	248	1	N/N	0.4	0.5	0.92	-0.2	148
2017/05/31 13:00	249	-3	N/N	0.36	0.55	0.89	-0.49	150
2017/06/01 07:06	217	-3	S/WU	2.2	0.35	0.81	0.29	389
2017/06/02 06:56	95	-3	VS/VS	-107.26	0.03	0.8	-0.45	60
2017/08/08 08:39	94	1	WS/N	0.01	0.44	0.91	-0.06	311
2017/08/08 13:06	91	-2	N/WS	-0.11	0.47	4.56	4.5	305
2017/08/09 08:34	219	0	VS/N	1.05	0.06	1.04	-0.18	471
2017/08/09 13:09	221	0	N/N	0.11	0.01	2.92	1.87	193
2017/08/10 10:49	217	0	VS/VU	11.4	0.37	0.92	-0.6	404
2017/08/14 10:08	93	-1	U/WU	-3.03	0.7	0.67	0.45	311
2017/08/14 14:40	94	-3	S/N	0.66	0.8	0.69	0.45	406
2017/08/15 07:22	124	-2	S/S	0.1	0.45	0.44	-0.09	250
2017/08/17 06:06	93	1	N/N	0.01	0.37	0.87	-0.54	235
2017/10/14 12:59	249	0	N/N	-0.04	0.19	2.14	1.91	408
2017/10/15 07:06	247	0	S/S	0.05	0.29	2.1	1.87	222
2017/10/15 11:52	121	-1	N/VS	-1.25	0.49	1.01	0.51	248

Other variables along the flight path, such as wind direction, temperature, specific humidity, and pressure, show good overall WRF performance (Fig. 6). Air pressure and specific humidity (although slightly higher in the observations on south-
 285 east side of the wake) show strong agreement between the observations and model. There is a cold bias (2–3 °C) in the WRF
 model predicted air temperature which is consistent across all 41 cases. Garcia-Diez et al. (2013) also found a cold bias all
 over Europe varying by season and time-of-day when relying on the MYJ PBL scheme. These slight biases, however, can be
 meaningful when considering factors such as wake path or atmospheric stability. Any model output error is especially
 important when considering the potential effects on a downstream wind farm, e.g., a slight error in wind direction can
 290 significantly impact the forecasted wind resource at the downwind farm.

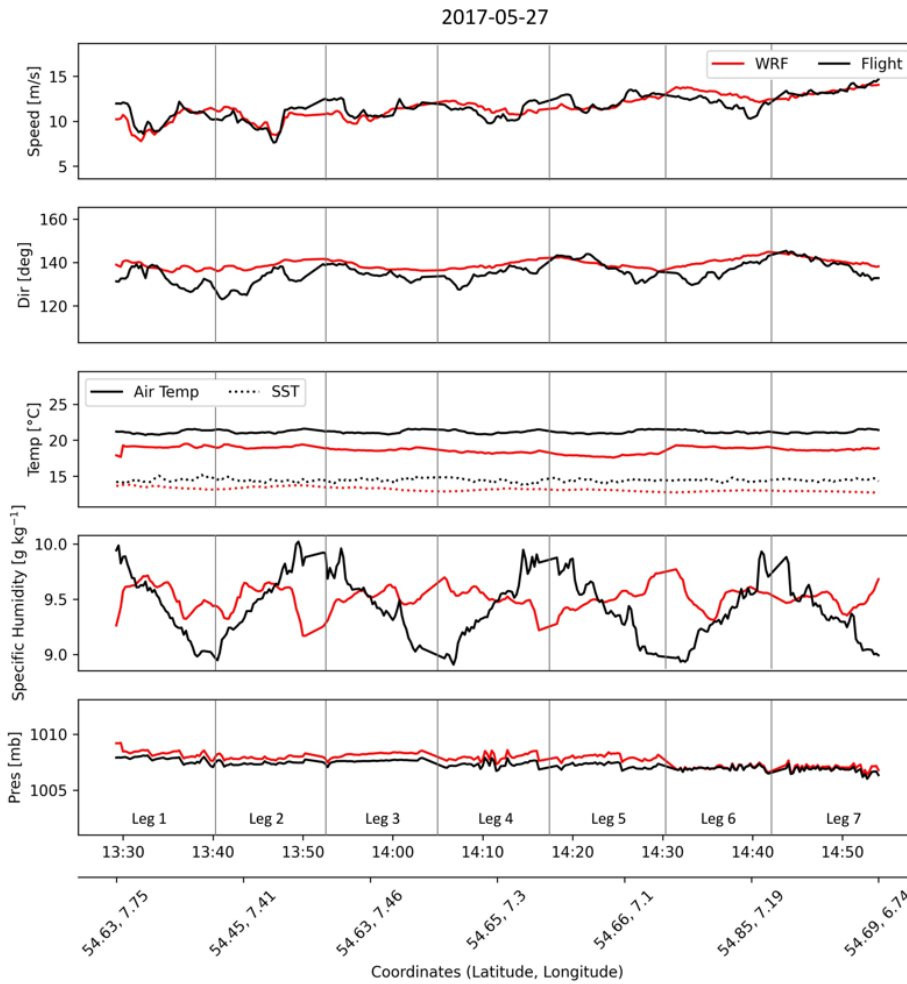


Figure 6: Timeseries of variables along flight track at 94 m AMSL. From top to bottom: wind speed (ms^{-1}), wind direction (degrees), Air temperature ($^{\circ}\text{C}$) and SST (dashed line), q (g kg^{-1}), and Air Pressure (mb) for flight observations (black) and corresponding WRF predictions (red). Grey vertical lines represent each horizontal flight leg, numbered 1–7, and shown along flight path in Fig. 4.

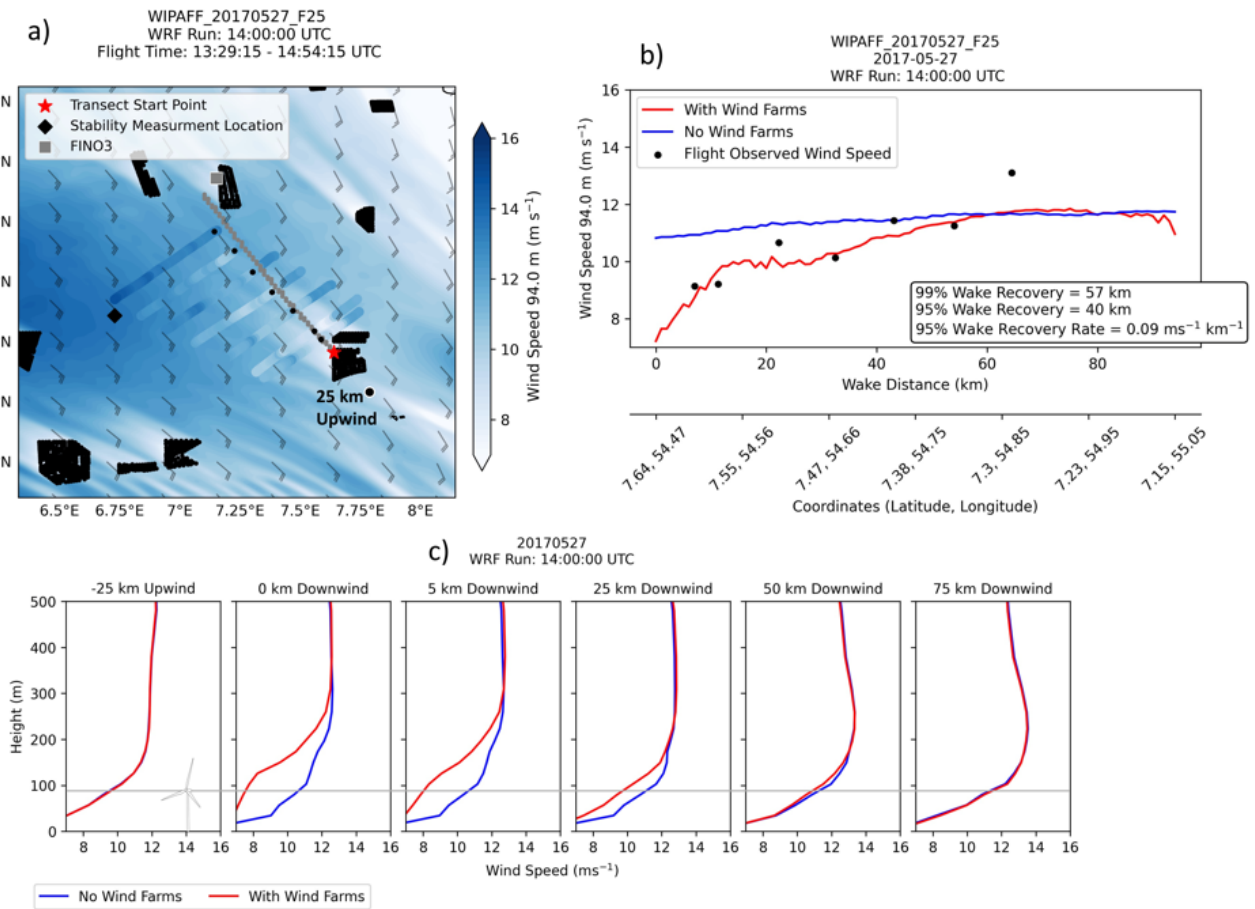
295

For example, on 27 May 2017, the wind direction bias is small (error ranges from 13.3° – -3.9° ; Fig. 6); however, the WRF wind direction is slightly more out of the south, contributing to a bias in the wake location (e.g., the difference between the black scatter points and the grey line as shown in Fig. 7a). WRF predicts the wake to be slightly offset towards the north than is observed from the aircraft (Fig. 7a). In most cases this will not impact wake length or deficit predictions, but it may change the alignment with another downwind farm. This is important, as depending on the wind array, properly modeling wind direction and alignment of wakes with downwind wind farms is crucial to accurate energy modeling. A long downwind wake is also observed during this event, as it takes 57 km before the wake recovers to the windspeed of the no-turbine (control)

300



WRF run (Fig. 7). The results are consistent with the observations (Fig. 7b) and with Cañadillas et al. (2020), who noted that
 305 wakes in the North Sea are found to extend over 50 km during stable conditions (Fig. 7b). On May 27 2017, Cañadillas et al.
 (2020) notes the observed 95% wake recovery length is 50 km compared to 40 km as shown in this WRF simulation (Fig. 7).
 This is confirmed by the observed 95% recovery wake length of 40 km on 6 September 2016 (Cañadillas et al. 2020) to WRF's
 value of 32 km (not shown). This introduces two questions: 1) is the WRF model able to properly estimate atmospheric stability
 offshore; and 2) is there a clear relationship between wake length and stability?
 310



315 **Figure 7: a) Contour plot of WRF 94-m wind field overlaid with flight wind speed measurements (ms⁻¹; approximate hub height, 94 m) for 27 May 2017 at 14 UTC (WRF) and 1429–1454 UTC (flight). Location of flight profile and stability calculations is shown by the black diamond. FINO3 tower location is shown in the grey square. Grey line indicates the downwind transect along the wake deficit. Black circle indicates a selected location 25 km upwind from the beginning of the transect (red star). Black scatter points downwind of wind farm represent downwind transect along the observed**



wind direction. b) Wind speed along wake transect for the no wind farm control run (blue) compared to the WRF run with wind farms (red) and the observed wind speed along the observed wind direction for each flight leg (black). c) Wind speed profiles before and after wind farm, shown along wake deficit transect comparing the no wind farm control run (blue) and run with wind farms (red). Grey horizontal line indicates approximate hub height, ~94 m AMSL.

4.2 Stability Analysis

Although atmospheric stability has been found to be integral in determining wake length, few studies have utilized observations to determine the ability of the WRF model to capture the near-surface stability offshore. Atmospheric profiles measured by the aircraft across the 41 WIPAFF case studies provide valuable measurements of the wind and thermodynamic profile offshore and provide us with a high spatial resolution of vertical measurements. Without aircraft flux measurements, L cannot be directly derived from observations and thus does not permit a direct comparison with WRF model output. The $\Delta T_{\text{Air-SST}}$ method is also inapplicable, as the measurements from the aircraft do not provide an ambient air temperature close enough to the surface (e.g., 2m or 10m). Therefore, we focus on calculations of Ri_b and δ (Eqs. 3 and 4).

Considering three different stability classifications for Ri_b (See Table 2) the Businger-Hicks Formulation results in a matching stability classification between the aircraft observations and corresponding WRF output more than 73% (Table 4) of the time, compared to 70% and 47% when using the Businger and Bulk Ri Formulations. A stability match is considered when the stability classification agrees within one stability class, e.g., Near-Stable and Stable or Near-Stable and Neutral. The Businger-Hicks formulation has the largest thresholds among different stability classes, making it less sensitive to small fluctuations in calculated Ri_b (Table 2).

Given the potential spatio-temporal biases in the flight profile, WRF's stability is also compared to measurements at the FINO3 tower. Note that in 2016 and 2017 the FINO3 tower, located adjacent to the DanTysk wind farm, provides *in situ* 10-min measurements of stability. From the flight data, stability is calculated between the lowest flight measurement and 100 m AMSL. The lowest aircraft profile measurement varies depending on the flight, ranging from 14 to 86 m AMSL, with an average profile start altitude of 44 m. Stability at the FINO3 tower is calculated between fixed measurement heights, 29 m and 95 m AMSL. WRF stability is calculated using the nearest available levels at the nearest grid point to both the location of the flight profile and FINO3 tower. For example, on 27 May 2017, stability at the flight profile location (Fig. 1) is calculated over a layer from 36 to 95 m AMSL and from 29 to 95 m at the FINO3 tower location. As shown, the profiles of wind speed, direction, and θ compare well with the concurrent WRF profile (Fig. 8). WRF underestimates wind speed and θ slightly; however, the shape and the stability of the profile is well represented (Fig. 8). When calculating Ri_b , the vertical gradients of wind speed and θ are most important (Eq. 3) and are shown to be better represented by the model when using thicker layers, such as the 36–102 m layer shown in this analysis (Fig. 8). However, when considering vertical gradients between each measurement height, the flight observations show stronger vertical gradients in wind speed, most apparent on 27 May 2017 at higher levels (> 100 m), resulting in WRF overestimating stability in this layer (Fig. 8).

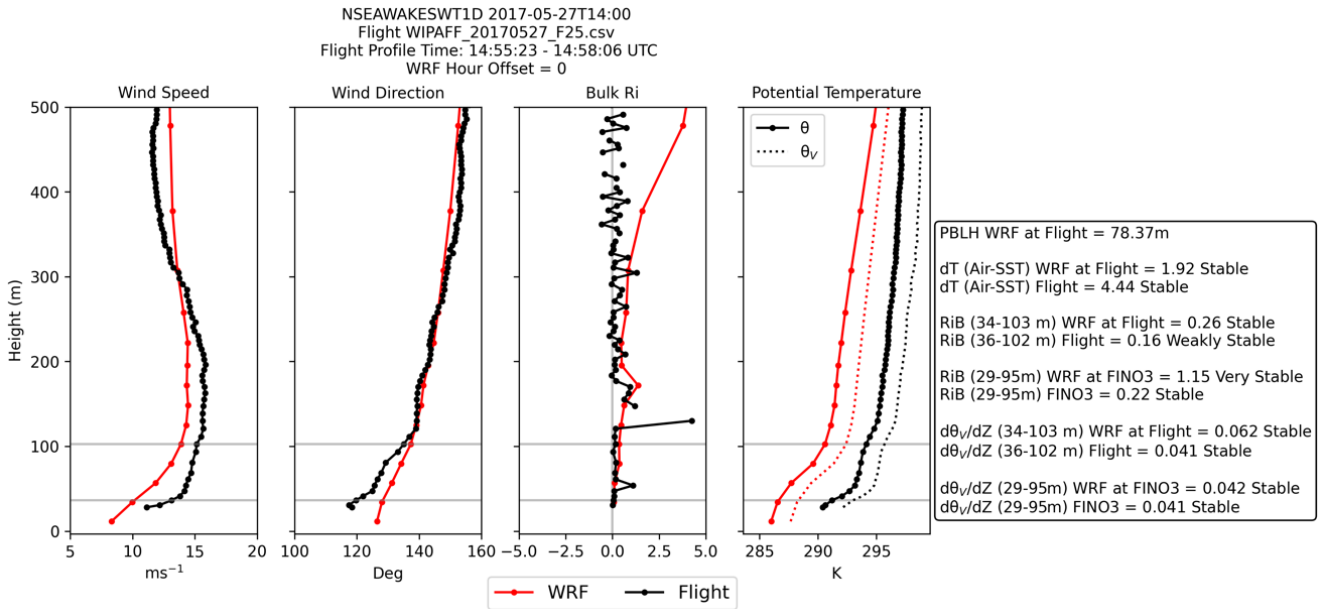
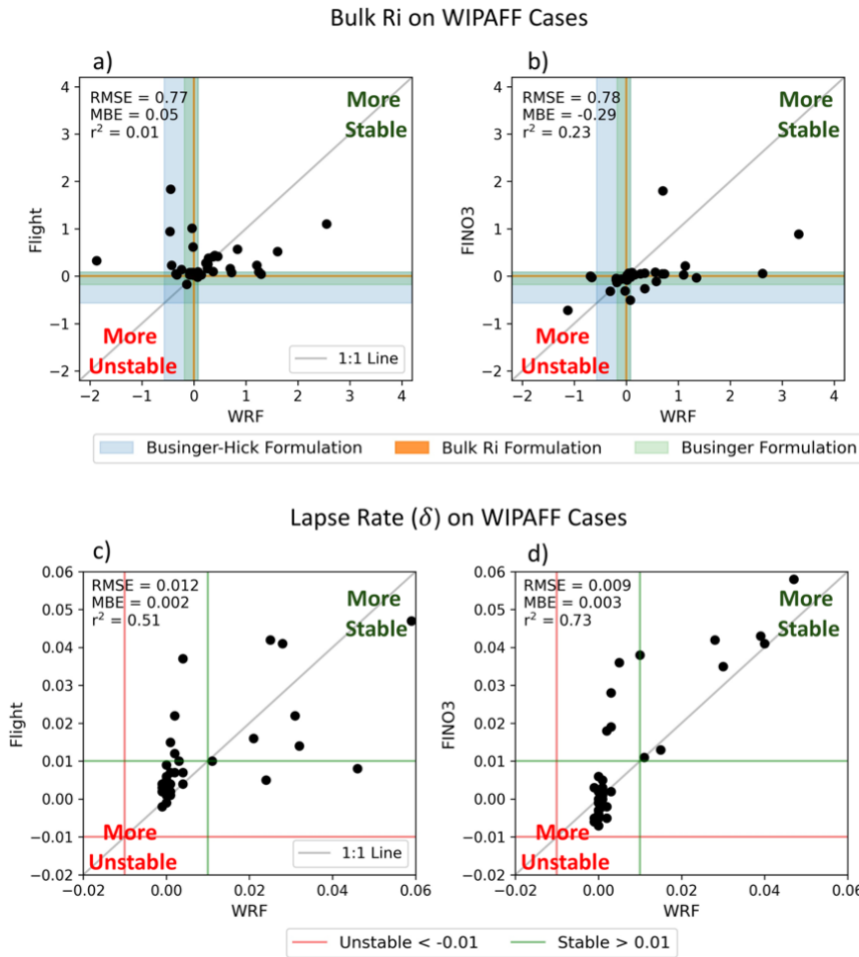


Figure 8: Profiles of wind speed (ms^{-1}), wind direction (deg), Ri_b , and θ (solid) and θ_v (dashed) for the flight observations (black) and corresponding WRF output (red). Metrics from WRF vs. Flight profile location and FINO3 location are summarized in text box on the right. Grey horizontal lines indicate levels of which metrics are calculated across.

355

As mentioned earlier, using the Businger-Hicks formulation to classify the Ri_b number into stability types indicates agreement between the WRF model and observations on 30 of the 41 flight cases. Classifying Ri_b into stability classes can be complicated, as results are dependent on the thresholds set for each stability class. For example, using the Businger-Hicks formulation gives a slightly different breakdown of stability across the 41 cases than applying the Bulk Ri Formulation (Table 2; Fig. 9a, b). However, overall, there is good agreement between the stability derived from the flights and the corresponding WRF runs (Table 4). Comparing the Ri_b and δ value at both the flight profile and FINO3 tower to the corresponding WRF forecast shows that the 41 cases compare well on the sign of Ri_b and δ (positive vs. negative) and that all WIPAFF flights experience near neutral to stable conditions (Fig. 9). One limitation of this dataset is the lack of extreme stability cases, so one cannot make conclusions on how wake activity will change during very stable or unstable conditions.

360



365

Figure 9: Scatter plot comparing a,b) Ri_b and c,d) δ from WRF (x-axis) to the measurements at Flight (y-axis; a,c) or FINO3 tower (y-axis; b,d). a-b) shaded areas represent the neutral threshold zone for the Businger-Hicks Formulation (blue), Bulk Ri Formulation (orange) and Businger formulation (green). 1 to 1 line is shown in grey. c-d) Green line indications stable threshold, red line indicates unstable threshold, and grey line indicates the 1 to 1 line.

370

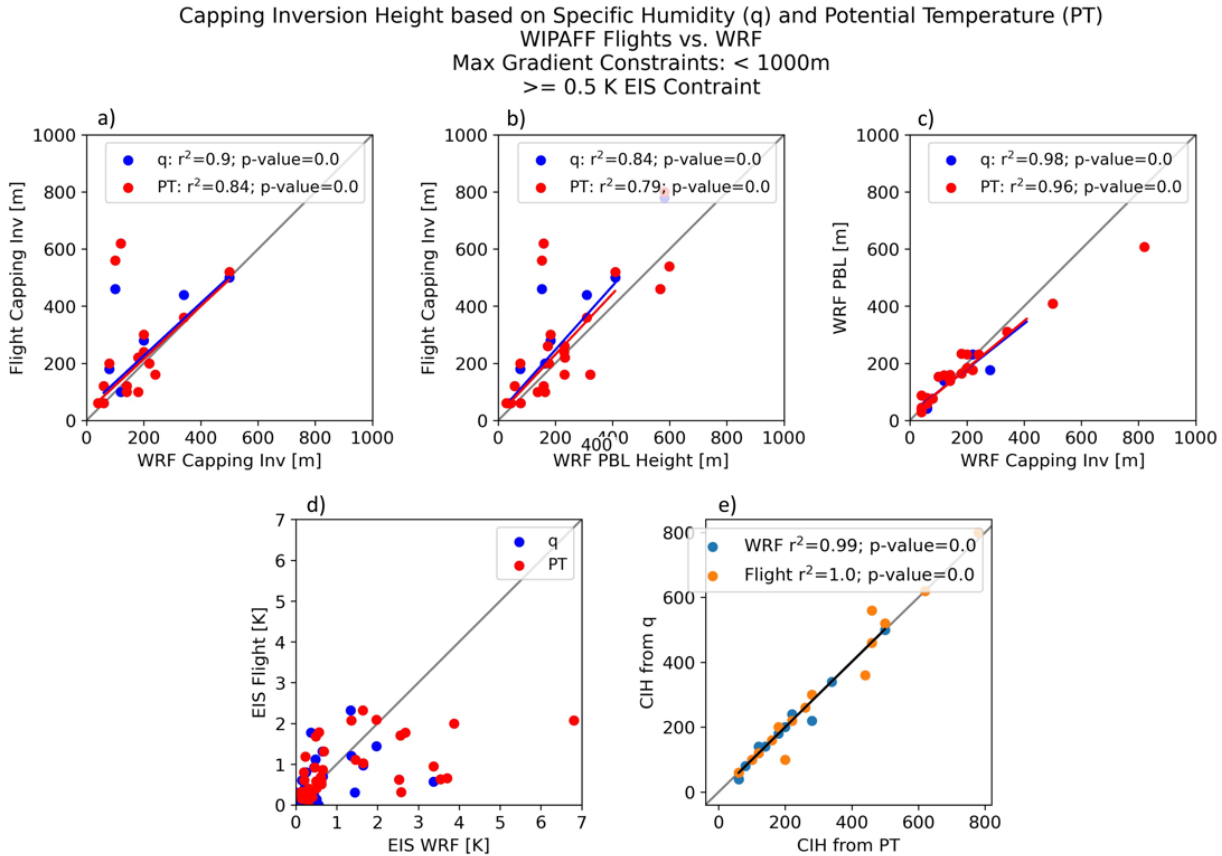
Despite some inconsistencies in the Ri_b stability classification, specifically the Businger-Hicks formulation, it serves as the best and most reliable metric to calculate stability offshore. Using δ results tend to overestimate the number of neutral cases (Fig. 9c, d).

In addition to validating WRF atmospheric stability regimes with the observations, we also evaluate WRF's ability to capture the CIH. Using the methods described in Section 3c, the CIH is calculated using the strongest gradients in the θ and q profiles. Using this method for all flight cases, it is found that that under stable conditions, the CIH derived from WRF and

375



from the observations, regardless of using θ or q to initially determine the height of the strongest gradient, compares well (Fig. 10).



380 **Figure 10: Regression analysis for WIPAFF profiles of a) Flight capping inversion to WRF capping inversion, b) Flight capping inversion compared to WRF PBL height, c) WRF PBL height compared to the WRF capping inversion, d) EIS derived from flight compared to EIS derived from WRF, for q (blue) and θ (red). Lastly, e) compares the CIH calculated from q compared to CIH calculated from θ for the flights (orange) and WRF (blue).**

385 Profiles of q and θ shown (Figure 11) for 2 flight cases illustrate these results. For example, 27 May 2017 is a stable case (Fig. 8) with a CIH of 60m (Fig. 11b). During stable events the CIH often falls within the rotor plane (generally between 60 to 120 m AMSL in the North Sea) and directional shear within the profile (especially apparent the aircraft data) is also observed (Fig. 11). For 6 September 2016, a neutral case, the profiles of q and θ from the flight and WRF model agree well, but there is not a definitive enough inversion within the profile to determine the CIH (Fig. 11a). However, based on analysis comparing

390 the CIH derived from WRF to the model estimated PBL height provided in the standard WRF output, the PBL height can used as a good approximation of the CIH when it cannot be explicitly calculated (Figs. 10b-c and 11).

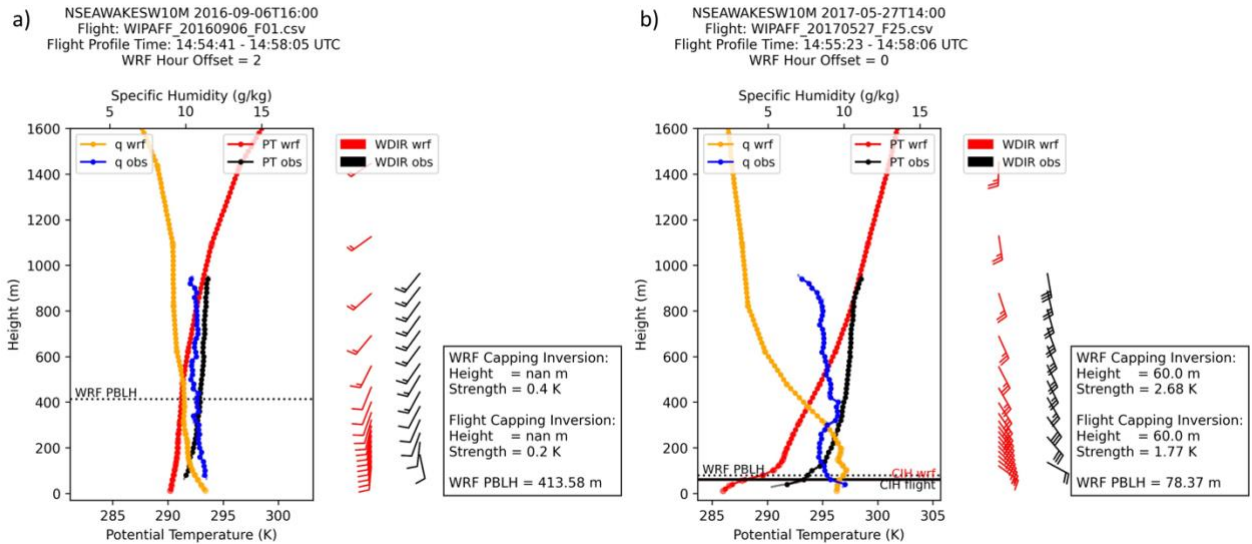
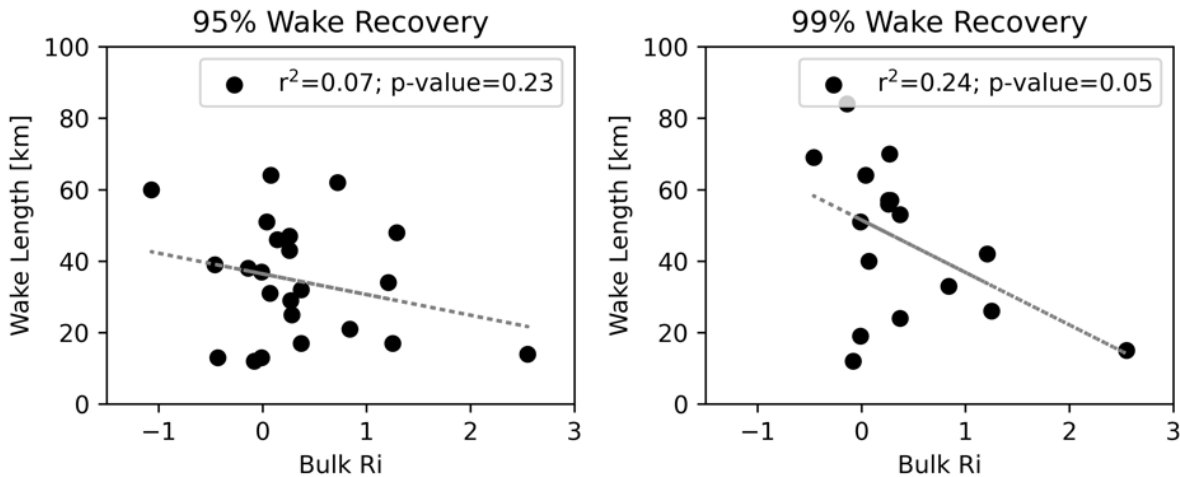


Figure 11: a) 6 September 2016 and b) 27 May 2017. Profiles of θ (bottom x-axis) from flight observations (black) compared to WRF (red) and profile of q (top x-axis) for flight observations (blue) compared to WRF (yellow). Wind barbs (1 full barb = 5 m s^{-1}) are shown for observations (black) and WRF (red). Also shown is the WRF PBL height (black dashed line), CIH from flight (solid black line) and WRF (solid red line). Values for PBL height, CIH, and EIS are summarized in the text box to right of plot.

4.3 Model Validation Summary

Model validation using the WIPAFF flight observations shows that under stable conditions the WRF model with the Fitch WFP parameterization well represents the wake behavior and atmospheric stability. Slight errors in wind direction are important to note, as they can change the downwind trajectory of the wake deficits. However, given the limited sampling of predominately stable and neutral cases, from this analysis it is not possible to confirm a robust relationship between wake length and stability regime (Fig. 12).



405

Figure 12: Regression (using r^2 , the coefficient of determination) analysis of WRF results comparing a) 95% wake recovery length (km) and b) 99% wake recovery length to Ri_b for 25 WIPAFF flights that measure the downwind wake at hub height.

410

This is consistent with the results in Cimini et al. (2025) that note prevailing offshore neutral conditions are a limitation when trying to understand model performance under offshore stability extremes (i.e. very unstable or very stable). While no linear relationship is found between the value of the Ri_b and the wake length for these selected cases, under stable conditions wakes are found to be upward of 50 km in length (Figs. 7 and 12), agreeing with claims in previous studies (Cañadillas et al. 2020; Ali et al. 2023; Hahmann et al. 2025).

415

Based upon comparison with thermodynamic profiles available from the aircraft data, the Ri_b derived from WRF can be used as a reliable metric to classify stability using the Businger-Hicks Formulation. Furthermore, the CIH derived from the WRF output, and the flight profile observations compare well. Comparing the PBL height from WRF's standard output to the CIH derived from WRF's thermodynamic profiles shows that, if necessary, the PBL height can be used as a rough estimate for CIH in offshore environments.

420

This is the first study to validate WRF model-derived Ri_b (and various classification performance) and CIH with observations in offshore regions. Using these results, Part II will discuss the overall climatology of the North Sea and how often long-range wake conditions may be expected.

5 Part II: North Sea Climatology

425

We next consider the annual stability regimes of the North Sea in the context of long-range wind farm wakes. After demonstrating the validity of using the WRF model to derive atmospheric stability, the WRF model can be leveraged to gain a better understanding of the annual distribution of near-surface stability. To do so, a 4-year WRF timeseries (2010–2013) is



run at the FINO3 tower in the North Sea (Fig. 2). Focus remains on the years 2010 through 2013, as this time period is prior to the development of nearby wind farms, including, Butendiek, DanTysk and Sandbank, and includes concurrent FINO3 tower data. Model setup follows the WRF configuration described in Table 1. Note that for this analysis, WRF is run with WFP off.

While the annual wind speed variability is small, the directional variability is apparent in Figure 13. Although the predominate wind direction is out of the western sector during all 4 years, 2010 features more north-west winds, while in 2011 the wind direction is commonly out of the west-south-west. This is confirmed by a change of 60° in the predominant wind direction between 2010 and 2011 (Fig. 13a-b). The annual mean SLP gradient for each year (not shown) shows 2010 to feature weaker gradients when compared to the other years (2011 and 2013 feature the strongest gradients). The WRF model captures this variability well, and accurately represents the wind rose when compared to observations (Fig. 13). Note that FINO tower observations are not assimilated into the ERA5 reanalysis and therefore do not impact the WRF hindcasts (Hersbach et al. 2020).

440

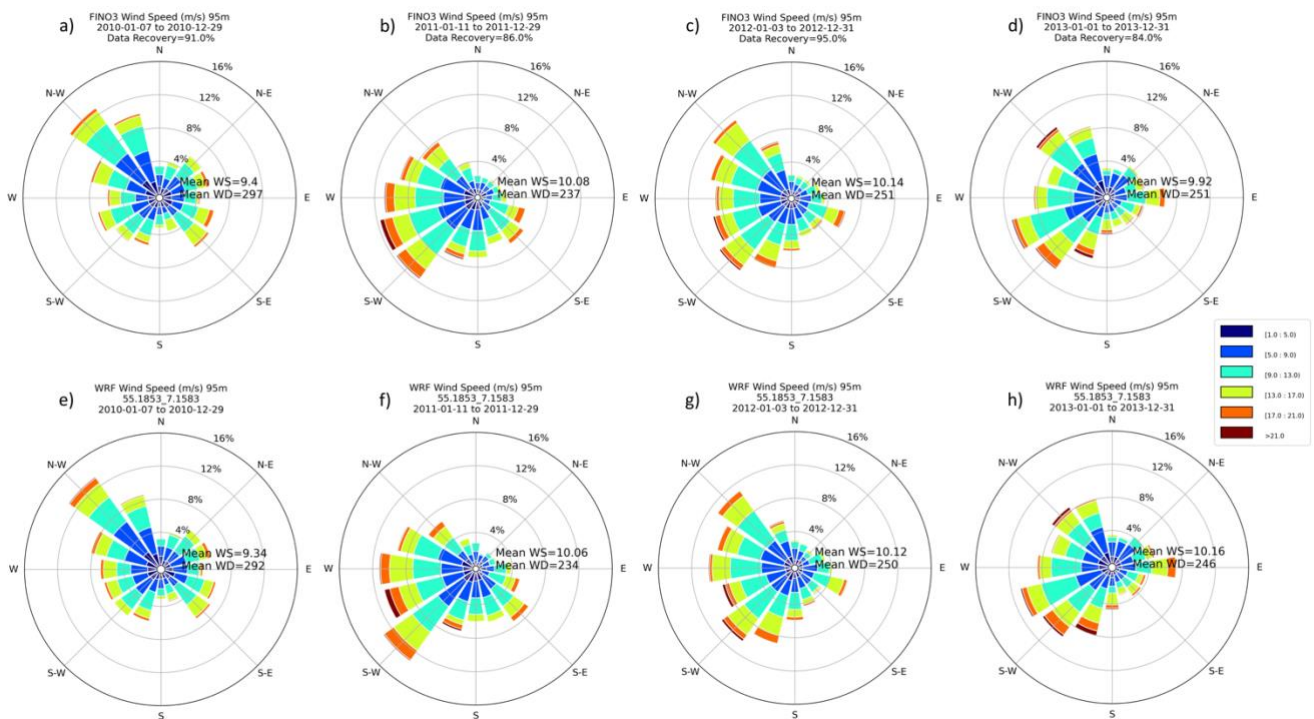
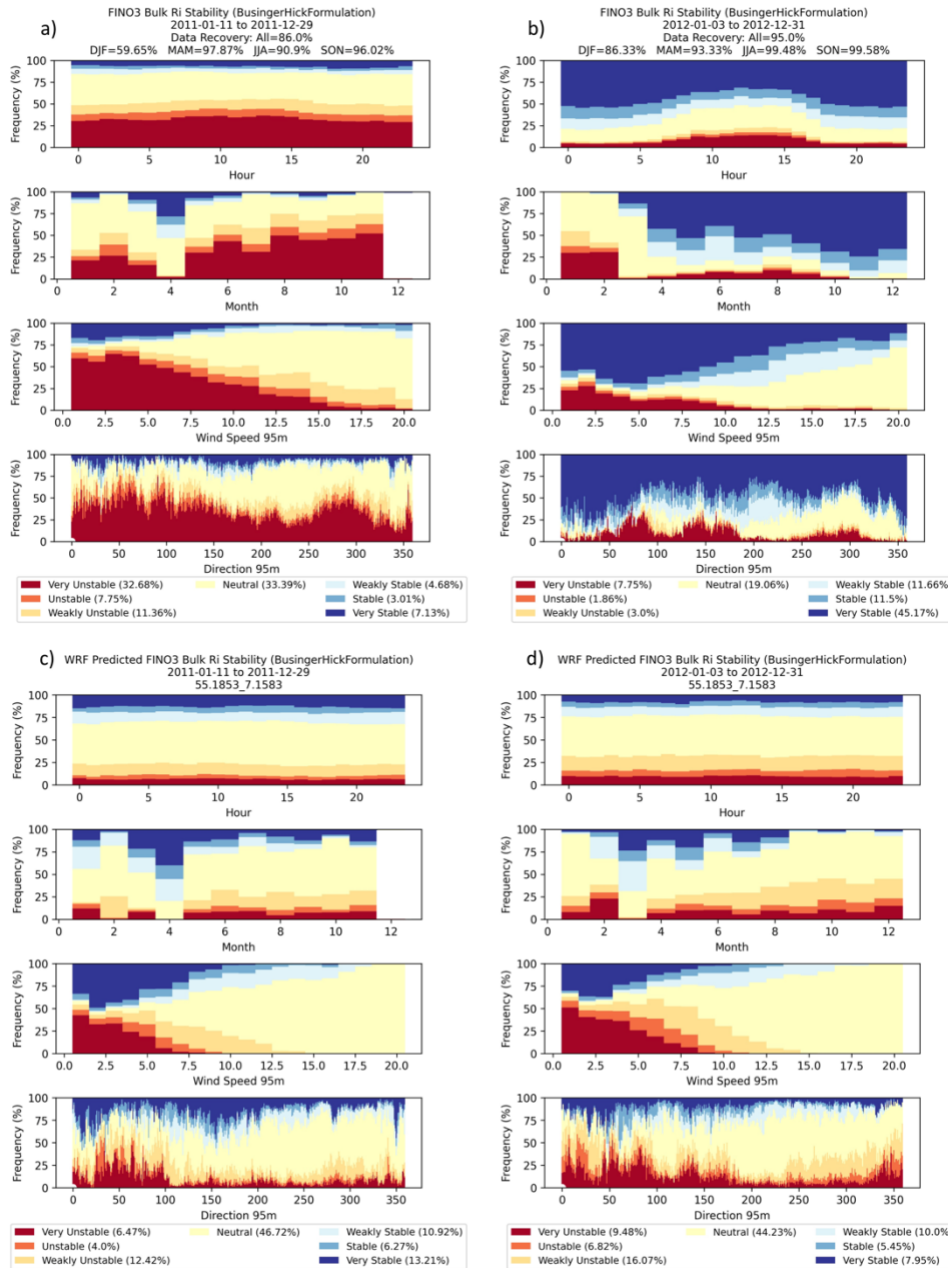


Figure 13: Annual composite wind roses for approximate hub height winds, 95 m, measured at the FINO3 tower for a) 2010, b) 2011, c) 2012, and d) 2013. Concurrent WRF wind rose is shown for e) 2010, f) 2011, g) 2012, and h) 2013. The radial labels indicate the frequency (%) at which the wind blows from that direction.

445



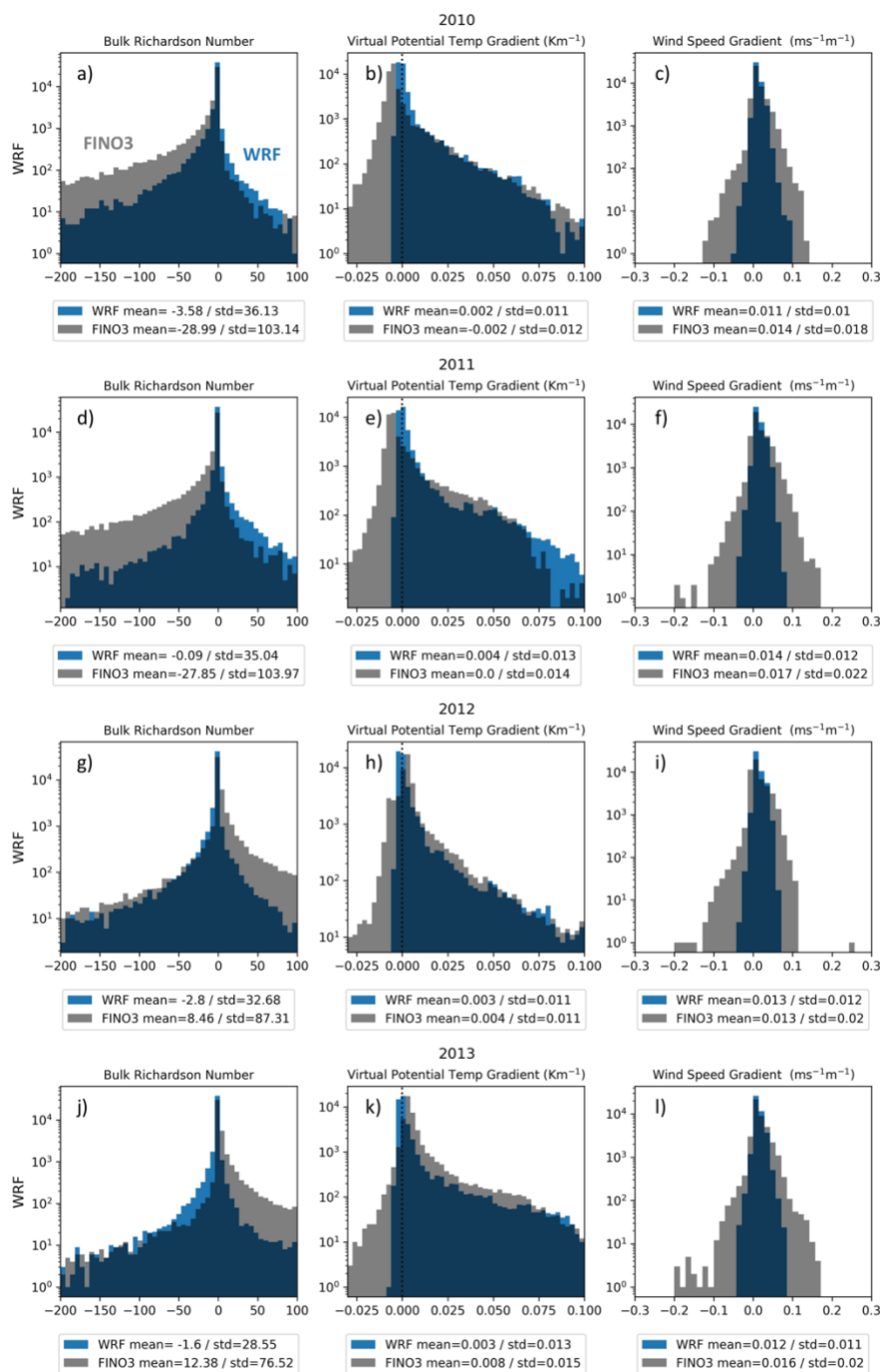
450 In addition to variability in the annual wind direction, rather significant year-to-year changes in stability are noted. Stability is determined using the Businger-Hicks Formulation for the Ri_b (Eq. 3; Table 2). Between 2011 and 2012 a shift is observed from more unstable to more stable conditions (Fig. 14a, b). Note the annual stability patterns in 2010 resemble 2011 with 2012 like 2013; therefore, only the years 2011 and 2012 are shown in Fig. 14. Interestingly, this shift is not seen by the concurrent WRF stability at the FINO3 tower location (Fig. 14c, d). However, both WRF and the FINO3 measurements indicate a high frequency of near neutral conditions (Fig. 14). Some discrepancies may be introduced into the data by the choice of Ri_b stability classification, as the numeric thresholds of the stability classes are tightly binned (as shown in Table 2).



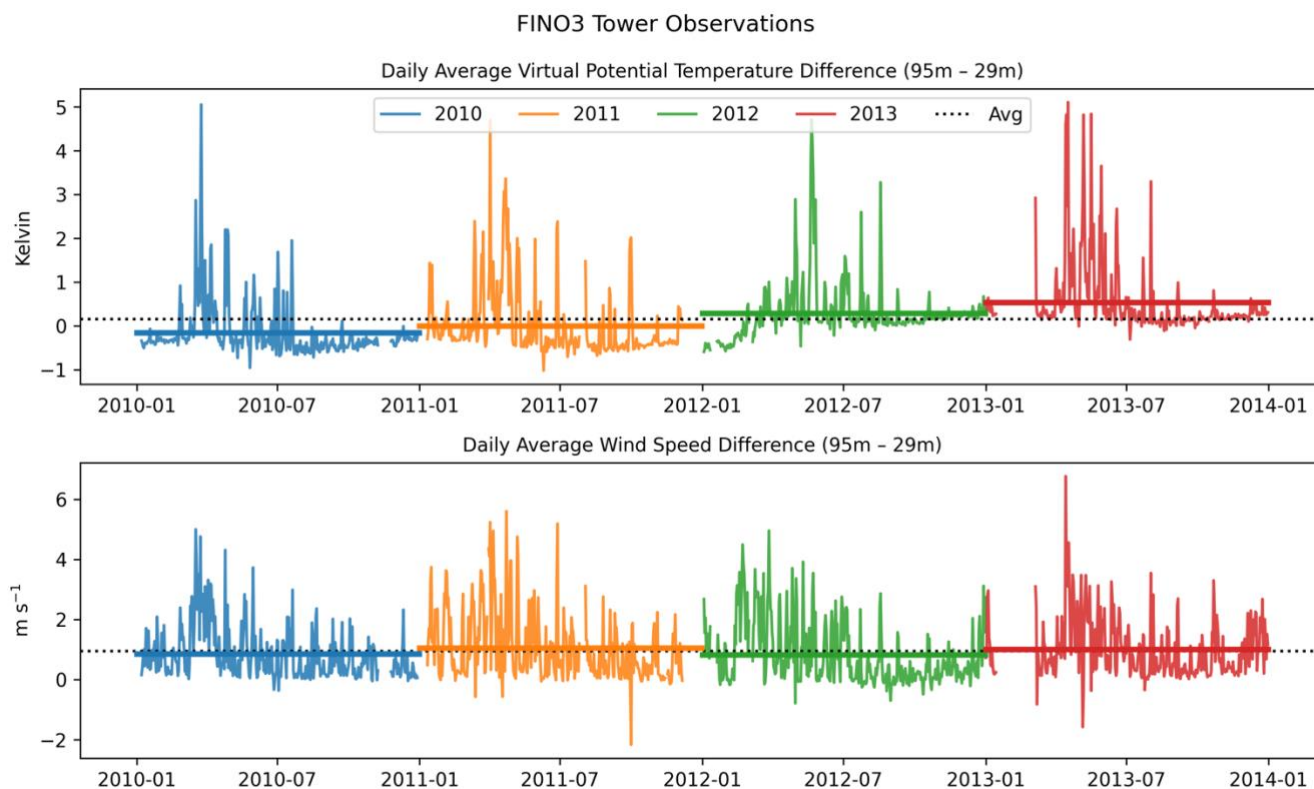
455 **Figure 14: Annual frequency (%) of Ri_b stability classes by the hour of day, month of year, wind speed, and wind direction for a, b) FINO3 tower observations and c, d) WRF concurrent time at FINO3 location. Results are shown for years 2011 (a, c) and 2012 (b, d). Note that December 2011 data are not available.**



460 For this reason, it is also important to consider the difference in stability from a statistical distribution perspective, as shown in Fig. 15. The histograms of the Ri_b value, calculated every 10-min between 29 and 95 m AMSL, confirm that 2012 and 2013 feature more frequent stable conditions when compared to 2010 and 2011. The stability shift is a direct result of increased values in the observed θ_v gradient between 2010 and 2011 to 2012 and 2013, whereas the vertical wind speed gradient stays consistent year-to-year (Figs. 15 and 16).



465 **Figure 15: Histograms of Ri_b (a, d, g, f), θ_v gradient ($K m^{-1}$; b, e, h, k), and wind speed gradient ($ms^{-1} m^{-1}$; c, f, i, l) between 29 m and 95 m. Observations (grey) are compared to the WRF prediction (blue) at FINO3 for a–c) 2010, d–f) 2011, g–i) 2012, and j–l) 2013.**



470 **Figure 16: Daily average difference in the θ_v (K; top) and the wind speed difference (m s^{-1} ; bottom) between 95 m and 29 m AMSL for 2010 (blue), 2011 (orange), 2012 (green) and 2013 (red). Solid colored lines indicate the annual average difference, black dashed line is the average difference across the 4-year period.**

475 However, regardless of stability classification, the same patterns of stability (seasonal, diurnal, wind regime) can be observed (Fig. 14). Unstable conditions are more common at lower wind speeds because of limited mixing (Fig. 14). Unstable conditions are also more frequent when winds are out of the east or south-east, which corresponds to a continental (Eurasian) air mass moving offshore (cold air moving over relatively warmer water). Overall, however, these results confirm that in the North Sea near neutral to stable conditions are most common, especially when considering winds speeds relevant to wind energy (above a cut in speed ~ 3 to 4 m s^{-1}).

480

6 Conclusions

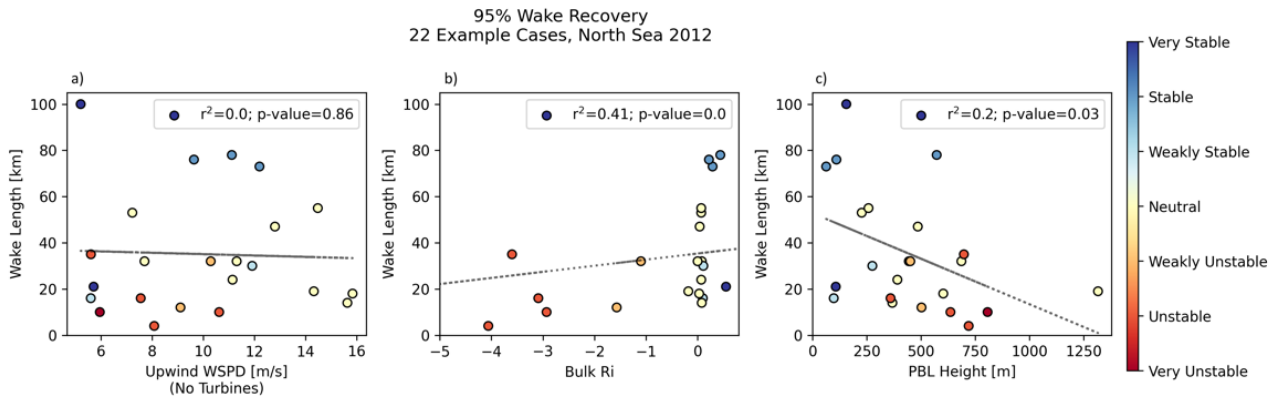


485 The work in this study focuses on the ability of the WRF model using the Fitch WFP to predict long-range offshore wind farm wakes. Although it is becoming widely accepted that wind farm wakes may propagate to downstream distances beyond 50 km under stable atmospheric conditions, little work has been done in offshore regions to validate these claims. As the analysis is presented in two parts, the results are summarized as follows:

490 1. The WIPAFF campaigns in 2016 and 2017 provided some of the first measurements of offshore wind farm waking, observed primarily during neutral and stable atmospheric conditions (Platis et al. 2018; Table 4). In this study, observations from the 41 WIPAFF flights and stationary measurements at the FINO3 tower are used to validate WRF's ability to predict long-range wakes behind large offshore wind farms. The results show that the model captures the wind speed deficit and wake length (commonly >50 km) well. However, there is a phase error in the WRF model of +/- 3 hours that is corrected for by shifting the WRF time stamp to best match with observations. Other variables along the flight path such as wind direction, temperature (slight cold bias), specific humidity, and pressure, show that overall WRF performance is good, but small wind direction errors are important to note as they can affect, for example, power production forecasting within and downwind of wind farms.

495 2. As thermal stability is critical to understanding wake length, the vertical thermodynamic profiles from the flights are used to evaluate WRF performance. We conclude that Ri_b derived from WRF can be used as a reliable metric to classify stability. Results show that in the offshore environment the Businger-Hicks formulation is most reliable. Furthermore, it is shown that the CIH derived from WRF model output and the flight profile observations compare well during stable conditions. Results also show that, when appropriate, the PBL height can be used as a rough estimate (Fig. 500 10c) for CIH in offshore environments.

505 3. Given the limitations of the data available from the WIPAFF flight campaign, this study focused on stable and neutral cases. A full year WRF simulation run over the North Sea region allows for a comparison of wake length to a wider range of stability classes. A subset of 22 cases is selected from the yearlong simulation run for 2012. These 22 days feature examples of unstable (7), neutral (8), and stable (7) conditions. Selecting examples during different stability regimes allows for analysis of the relationship between wind speed, Ri_b and PBL height to the length of the external wind farm wake. As demonstrated, there is no relationship between wind speed and wake length (Fig. 17). However, these results confirm the hypothesis that more stable cases will result in longer wakes (Fig. 17). Also, a lower PBL height is often indicative of more stable conditions, and therefore, longer wakes (Fig. 17).



510 **Figure 17: Regression (using r^2 , the coefficient of determination) analysis of WRF results comparing wake length (km) to a) wind farm upwind wind speed (ms^{-1}) b) Ri_b value and c) PBL height (m). Points (open circles) are color coded by stability class.**

4. To further understand the met-ocean climatology of the North Sea in the context of offshore wind energy, particularly how often the region can expect long-range wakes, the in-situ measurements at the FINO3 tower are compared to the WRF model over a 4 year period (2010–2013; prior to when the FINO3 mast was surrounded by operational wind farms). Results show that the North Sea region experiences significant annual variation in the wind direction and stability (Figs. 13 and 14). However, overall, the North Sea met-ocean environment is characterized by mostly neutral and near-neutral conditions.

515 This is the first study to validate WRF model derived Ri_b and CIH using observed thermodynamic profiles in offshore regions. The findings in this study can be applied to other regions with existing wind farms or undergoing offshore wind energy development, and can facilitate establishing a robust climatology of wind regimes and stability, providing a better understanding of conditions favorable for long-range wind farm wakes.

Data availability

525 Information on the FINO towers can be found and downloaded at: https://www.bsh.de/DE/DATEN/daten_node.html.
The WIPAFF flight data can be found and downloaded at: <https://doi.pangaea.de/10.1594/PANGAEA.903088>.

Author contributions

JF, PB, and EM conceptualized the project and obtained funding and resources for the work. PB and NR provided the data, EM processed the data used for model evaluation and performed the WRF simulations with the assistance of PB and AG. EM conducted the analysis, produced the figures, and interpreted results with supervision and input from PB, JF, and NR. EM prepared the initial draft and all authors reviewed and edited the publication.

Competing interests



535 The authors declare that they have no conflict of interest.

Disclaimer

The views expressed in the article do not necessarily represent the views of the NSF or the US government.

540 Acknowledgements

This work utilized the computing resources at UL Solutions and the Atmospheric Sciences Research Center (ASRC) at the University at Albany. Data storage was supported by UL Solutions and ASRC. Funding was provided by National Science Foundation (NSF) through a funded internship program.

545 Financial support

This research was funded by the National Science Foundation Internship Program Fellowship, award number 1183904-2-98042.

References

- 550 Ali, K., Schultz, D. M., Revell, A. Stallard, T., & Ouro, P., 2023: Assessment of Five Wind-Farm Parameterizations in the Weather Research and Forecasting Model: A Case Study of Wind Farms in the North Sea. *Monthly Weather Review*, **151**, 2333–2359, <https://doi.org/10.1175/MWR-D-23-0006.1>.
- Archer, C. L., Colle, B. A., Veron, D. L., Veron, F., & Sienkiewicz, M. J., 2016: On the predominance of unstable atmospheric conditions in the marine boundary layer offshore of the U.S. northeastern coast, *Journal of Geophysical Research: Atmospheres*, **121**, 8869–8885, <https://doi.org/10.1002/2016JD024896>.
- 555 Archer, C. L., Wu, S., Ma, Y., & Jiménez, P., 2020: Two corrections for turbulent kinetic energy generated by wind farms in the WRF Model. *Monthly Weather Review*, **148**, 4823–4835, <https://doi.org/10.1175/MWR-D-20-0097.1>.
- Ball, F. K., 1960: Control of inversion height by surface heating. *Quart. J. Roy. Meteor. Soc.*, **86**, 483–494, <https://doi.org/10.1002/qj.49708637005>.
- 560 Barthelmie, R. J., 1999: The effects of atmospheric stability on coastal wind climates. *Meteorological Applications*, **6**, 39–47, <https://doi.org/10.1017/S1350482799000961>.
- Berge, K., Centurelli, G., Dörenkämper, M., Bange, J., Platis, A., 2024: Evaluation of Engineering Models for Large-Scale Cluster Wakes With the Help of In Situ Airborne Measurements. *Wind Energy*, **27**, 1040–1062, <https://doi.org/10.1002/we.2942>.
- 565 Brower, M., & Robinson, N., 2009: The openwind deep-array wake model: development and validation. Technical report from AWS Truepower, Albany, NY, 15pp, https://www.ul.com/sites/default/files/2024-11/UL_Solutions_Deep-Array-Wake-Model_Validation_2024.pdf.



- Cañadillas, B., & coauthors, 2020: Offshore wind farm wake recovery: Airborne measurements and its representation in engineering models. *Wind Energy*, **23**(5), 1165–1366, <https://doi.org/10.1002/we.2484>.
- 570 Cañadillas, B., Beckenbauer, M., Trujillo, J. J., Dörenkämper, M., Foreman, R., Neumann, T., & Lampert, A., 2022: Offshore wind farm cluster wakes as observed by long-range-scanning wind lidar measurements and mesoscale modeling. *Wind Energy Science*, **7**, 1241–1262. <https://doi.org/10.5194/wes-7-1241-2022>.
- Cantero, E., Sanz, J., Borbon, F., Paredes, D., & Garcia, A., 2022: On the measurement of stability parameters over complex mountainous terrain. *Wind Energy Science*, **7**, 221–235.
- 575 Christiansen, M. B., & Hasager, C. B., 2005: Wake effects of large offshore wind farms identified from satellite SAR. *Remote Sens. Environ.*, **98**, 251–268, <https://doi.org/10.1016/j.rse.2005.07.009>.
- Christiansen, M. B., & Hasager, C. B., 2006: Using airborne and satellite SAR for wake mapping offshore. *Wind Energy*, **9**, 437–455, <https://doi.org/10.1002/we.196>.
- Cimini, D., & coauthors, 2025: Atmospheric stability from numerical weather prediction models and microwave radiometer observations for onshore and offshore wind energy applications. *Atmospheric Measurement Techniques*, **18**, 2041–2067, <https://doi.org/10.5194/amt-18-2041-2025>.
- 580 Corsmeier, U., Hankers, R., & Wieser, A., 2001: Airborne turbulence measurements in the lower troposphere onboard the research aircraft Dornier 128-6, D-IBUF. *Meteorologische Zeitschrift*, **10**(4), 315–329, <https://doi.org/10.1127/0941-2948/2001/0010-0315>.
- Deardorff, J. W., 1979: Prediction of convective mixed-layer entrainment for realistic capping inversion structure. *Journal of the Atmospheric Sciences*, **36**, 424–436. [https://doi.org/10.1175/1520-0469\(1979\)036<0424:POCMLE>2.0.CO;2](https://doi.org/10.1175/1520-0469(1979)036<0424:POCMLE>2.0.CO;2).
- 585 Debnath, M., & coauthors, 2022: Design of the American Wake Experiment (AWAKEN) field campaign. *Journal of Physics*, **2265**(022058), <https://doi.org/10.1088/1742-6596/2265/2/022058>.
- Djath, B., Schulz-Stellenfleth, J. & Cañadillas, B., 2018: Impact of atmospheric stability on X-band and C-band Synthetic Aperture Radar imagery of offshore windpark wakes. *Journal of Renewable and Sustainable Energy*, **10**, <https://doi.org/10.1063/1.5020437>.
- 590 Djath, B., Schulz-Stellenfleth, J., & Cañadillas, B., 2022: Study of Coastal Effects Relevant for Offshore Wind Energy Using Spaceborne Synthetic Aperture Radar (SAR). *Remote Sensing*, **14**(7), 1688. <https://doi.org/10.3390/rs14071688>.
- European Centre for Medium-Range Weather Forecasts (ECMWF), 2019: Global reanalysis: goodbye ERA-Interim, hello ERA5. Accessed 21 March 2023, <https://www.ecmwf.int/en/newsletter/159/meteorology/global-reanalysis-goodbye-era-interim-hello-era5>.
- 595 Fischereit, J., Brown, R., Larsén, X. G., Badger, J., & Hawkes, G., 2021: Review of Mesoscale Wind-Farm Parametrizations and Their Applications, *Boundary Layer Meteorology*, **182**, 175–224, <https://doi.org/10.1007/s10546-021-00652-y>.
- Fischereit, J., Hansen, K. S., Larsén, X. G., van der Laan, M. P., Réthoré, P., & Leon, J. P. M., 2022: Comparing and validating intra-farm and farm-to-farm wakes across different mesoscale and high-resolution wake models. *Wind Energy Science*, **7**, 1069–1091, <https://doi.org/10.5194/wes-7-1069-2022>.
- 600



- Fitch, A. C., Olson, J. B., Lundquist, J. K., Dudhia, J., Gupta, A. K., Michalakes, J., & Barstad, I., 2012: Local and Mesoscale Impacts of Wind Farms as Parameterized in a Mesoscale NWP Model. *Monthly Weather Review*, **140**, 3017–3038, <https://doi.org/10.1175/MWR-D-11-00352.1>.
- 605 Floors, R., Gryning, S., Peña, A., & Batchvarova, E., 2011: Analysis of diabatic flow modification in the internal boundary layer. *Meteorologische Zeitschrift*, **20**(6), 649–659, <https://doi.org/10.1127/0941-2948/2011/0290>.
- Foreman, R. J., Cañadillas, B., & Robinson, N., 2024: The Atmospheric Stability Dependence of Far Wakes on the Power Output of Downstream Wind Farms. *Energies*, **17**(2), 488. <https://doi.org/10.3390/en17020488>.
- García-Díez, M., Fernández, J., Fita, L., & Yagüe, C., 2013: Seasonal dependence of WRF model biases and sensitivity to PBL schemes over Europe. *Quarterly Journal of the Royal Meteorological Society*, **139**(671), 501–514. <https://doi.org/10.1002/qj.1976>.
- 610 Garstang, M., and D. R. Fitzjarrald, 1999: Observations of Surface to Atmosphere Interactions in the Tropics. Oxford University Press, 405 pp.
- Golbazi, M., Archer, C., & Alessandrini, S., 2022: Surface impacts of large offshore wind farms. *Environmental Research Letter*, **17**, <https://doi.org/10.1088/1748-9326/ac6e49>.
- 615 Gunnerson, C. G., 1981: The New York Bight ecosystem. Marine Environmental Pollution, 2: Dumping and Mining, R. A. Geyer, Ed., Elsevier Oceanography Series, Vol. 27, Elsevier, 313–378.
- Hahmann, A. N., Imberger, M., Fischereit, J., Alonso-de-Linaje, N. G., & Badger, J., 2025: Environmental Mapping and Screening of the Offshore Wind Potential in Denmark: Sensitivity mapping: Wind. DTU Wind and Energy Systems.
- Hansen, K. S., Barthelmie, R. J., Jensen, L. E., and Sommer, A. 2012: The impact of turbulence intensity and atmospheric stability on power deficits due to wind turbine wakes at Horns Rev wind farm. *Wind Energy*, **15**, 183–196, <https://doi.org/10.1002/we.512>.
- 620 Hasager, C. B., Vincent, P., Badger, J., Badger, M., Di Bella, A., Peña, A., Husson, R., & Volker, P. J. H., 2015: Using Satellite SAR to Characterize the Wind Flow around Offshore Wind Farms. *Energies*, **8**, <https://doi.org/10.3390/en8065413>.
- Hersbach, H., & Coauthors, 2020: The ERA5 global reanalysis. *Quarterly Journal of the Royal Meteorological Society*, **625** **146**(730), 1999–2049, <https://doi.org/10.1002/qj.3803>.
- Kihlström, L., 2023: How Horns Rev 1 paved the way for offshore wind. Vattenfall, Accessed 5 May 2025, <https://group.vattenfall.com/press-and-media/newsroom/2023/how-horns-rev-1-paved-the-way-for-offshore-wind>.
- Krishnamurthy, R., & coauthors, 2024: Observations of wind farm wake recovery at an operating wind farm. *Wind Energy Science*, **10**(2), 361–380, <https://doi.org/10.5194/wes-10-361-2025>.
- 630 Lundquist, J. K., DuVivier, K. K., Kaffine, D., Tomaszewski, J. M., 2019: Costs and consequences of wind turbine wake effects arising from uncoordinated wind energy development. *Nature Energy*, **4**, 26–34, <https://doi.org/10.1038/s41560-019-0363-9>.



- Ma, Y., Archer, C. L., & Vassel-Be-Hagh, A., 2022: Comparison of individual versus ensemble wind farm parameterizations inclusive of sub-grid wakes for the WRF model. *Wind Energy*, **25**(9), <https://doi.org/10.1002/we.2758>.
- 635 McCabe, E. J., & Freedman, J. M., 2025: Quantifying the uncertainty in the weather research and forecasting model under sea breeze and low-level jet conditions in the New York Bight: Importance to offshore wind energy. *Weather and Forecasting*, **40**(3), <https://doi.org/10.1175/WAF-D-22-0119.1>.
- Mohan, M. & Siddiqui, T. A., 1998: Analysis of various schemes for the estimation of atmospheric stability classification. *Atmospheric Environment*, **32**(21), 3775–3781.
- 640 Monin, A. S., & Obukhov, A. M., 1954: Basic laws of turbulent mixing in the surface layer of the atmosphere. *Tr. Akad. Nauk SSSR Geophys. Inst*, **24**(151), 163–187.
- Nakanishi, M. & Niino, H., 2006: An Improved Mellor-Yamada Level 3 Model: Its Numerical Stability and Application to a Regional Prediction of Advection Fog. *Boundary-Layer Meteorology*, **119**, 397-407, <http://dx.doi.org/10.1007/s10546-005-9030-8>.
- 645 Nakanishi, M., and H. Niino, 2009: Development of an improved turbulence closure model for the atmospheric boundary layer. *J. Meteor. Soc. Japan*, **87**, 895–912, doi:10.2151/jmsj.87.895.
- National Renewable Energy Laboratory (NREL), 2022. The American WAKE experiment (AWAKEN): Groundbreaking International Field Research Addresses Wind Farm Atmospheric Interactions. <https://www.energy.gov/sites/default/files/2022-01/AWAKEN-fact-sheet.pdf>
- 650 Nygaard, N. G., Steen, S. T., Poulsen, L., Pedersen, J. G., 2020: Modelling cluster wakes and wind farm blockage. *Journal of Physics: Conference Series*, **1618**, 062072, <https://doi.org/10.1088/1742-6596/1618/6/062072>.
- Olsen, B. T., Hahmann, A. N., Sempreviva, A. M., Badger, J., and Jørgensen, H. E., 2017: An intercomparison of mesoscale models at simple sites for wind energy applications. *Wind Energy Science*, **2**, 211–228, <https://doi.org/10.5194/wes-2-211-2017>.
- 655 Olson, J. B., J. S. Kenyon, W. A. Angevine, J. M. Brown, M. Pagowski, and K. Sušelj, 2019: A description of the MYNN EDMF scheme and the coupling to other components in WRF–ARW. NOAA Tech. Memo. OAR GSD 61, 42 pp., <https://doi.org/10.25923/n9wm-be49>.
- Ørsted, 2019: Making green energy affordable. 28 pp, <https://orsted.com/-/media/WWW/Docs/Corp/COM/explore/Making-green-energy-affordable-June-2019.pdf>.
- 660 Pedersen, J. G., Svensson, E., Poulsen, L., Nygaard, N. G., 2022: Turbulence Optimized Park model with Gaussian wake profile. *Journal of Physics: Conference Series*, **2265**, <https://doi.org/10.1088/1742-6596/2265/2/022063>.
- Platis, A. & coauthors, 2018: First in situ evidence of wakes in the far field behind offshore wind farms. *Scientific Reports*, **8**(2163), <https://doi.org/10.1038/s41598-018-20389-y>.
- 665 Platis, A., & coauthors, 2020: Long-range modifications of the wind field by offshore wind parks – results of the project WIPAFF. *Meteorologische Zeitschrift*, **29**(5), 355–367, <https://doi.org/10.1127/metz/2020/1023>.



- Porchetta, S., Howland, M. F., Borgers, R., Buckingham, S., & Munters, W., 2024: Annual wake impacts in and between wind farm clusters modelled by a mesoscale numerical weather prediction model and fast-running engineering models. *Wind Energy Science*, preprint, <https://doi.org/10.5194/wes-2024-58>.
- 670 Pryor, S. C. & Barthelmie, R. J., 2024: Power Production, Inter- and Intra-Array Wake Losses from the U.S. East Coast Offshore Wind Energy Lease Areas, *Energies*, **17**(1063), <https://doi.org/10.3390/en17051063>.
- Pronk, V., Bodini, N., Optis, M., Lundquist, J. K., Moriarty, P., Draxl, C., Purkayastha, A., and Young, E. 2022: Can reanalysis products outperform mesoscale numerical weather prediction models in modeling the wind resource in simple terrain? *Wind Energy Science*, **7**, 487–504, <https://doi.org/10.5194/wes-7-487-2022>.
- 675 Rausch, T., & Coauthors, 2023: In-situ airborne measurements of atmospheric and sea surface parameters related to offshore wind parks in the German Bight [dataset publication series]. *PANGAEA*, <https://doi.org/10.1594/PANGAEA.955382>.
- Rampanelli, G., & Zardi D., 2004: A Method to Determine the Capping Inversion of the Convective Boundary Layer. *Journal of Applied Meteorology and Climatology*, **43**, 925–933, [https://doi.org/10.1175/1520-0450\(2004\)043<0925:AMTDTC>2.0.CO;2](https://doi.org/10.1175/1520-0450(2004)043<0925:AMTDTC>2.0.CO;2).
- 680 Rogers, J. D., 2024: Experimental evaluation of wind turbine wake turbulence impacts on a general aviation aircraft, *Wind Energy Science*, **9**, 1849–1868, <https://doi.org/10.5194/wes-9-1849-2024>.
- Rosencrans, D., Lundquist, J. K., Optis, M., Rybchuk, M., Bodini, N., & Rossol, M., 2024: Seasonal variability of wake impacts on US mid-Atlantic offshore wind plant power production. *Wind Energy Science*, **9**, 555–583, <https://doi.org/10.5194/wes-9-555-2024>.
- 685 Ruisi, R. & Bossanyi, E., 2019: Engineering models for turbine wake velocity deficit and wake deflection. A new proposed approach for onshore and offshore applications. *Journal of Physics*, Conf. Series 1222.
- Skamarock, W. C., & Coauthors, 2021: A Description of the Advanced Research WRF Model Version 4.3, NCAR/TN-556+STR, Mesoscale and Microscale Meteorology Division, National Center for Atmospheric Research, Boulder, doi:10.5065/1dfh-6p97.
- 690 Stoelinga, M., Sanchez-Gomez, M., Poulos, G., Crescenti, J., 2022: Estimating Long-Range External Wake Losses in Energy Yield and Operational Performance Assessments Using the WRF Wind Farm Parameterization. Technical report from ArcVera, 19 pp, <https://arcvera.com/wp-content/uploads/2022/08/ArcVera-White-Paper-Estimating-Long-Range-External-Wake-Losses-WRF-WFP-1.0.pdf>.
- Stull, R. B., 1988: An Introduction to Boundary Layer Meteorology. Kluwer Academic Publishers.
- 695 Tennekes, H., 1973: A Model for the Dynamics of the Inversion Above a Convective Boundary Layer. *Journal of the Atmospheric Sciences*, **30**, 558–567, [https://doi.org/10.1175/1520-0469\(1973\)030<0558:AMFTDO>2.0.CO;2](https://doi.org/10.1175/1520-0469(1973)030<0558:AMFTDO>2.0.CO;2).
- Vattenfall, 2025: Horns Rev 1. Accessed 5 May 2025, <https://powerplants.vattenfall.com/horns-rev/>.
- Wang, Z., Yuan, J., Wood, R., Chen, Y., & Tong, T., 2023: Profile-based estimated inversion strength. *Atmospheric Chemistry and Physics*, **23**, 3247–3266, <https://doi.org/10.5194/acp-23-3247-2023>.



- 700 Wood, R., and C. S. Bretherton, 2006: On the Relationship between Stratiform Low Cloud Cover and Lower-Tropospheric Stability. *Journal of Climate*, **19**, 6425–6432, <https://doi.org/10.1175/JCLI3988.1>.
- Xia, G., Cervarich, M. C., Roy, S. B., Zhou, L., Minder, J. R., Jimenez, P. A., & Freedman, J. M., 2017: Simulating Impacts of Real-World Wind Farms on Land Surface Temperature Using the WRF Model: Validation with Observations. *Monthly Weather Review*, **145**, 4813–4836, <https://doi.org/10.1175/MWR-D-16-0401.1>.
- 705 Zhan, L., Letizia, S. & Iungo, G. V., 2020: Optimal tuning of engineering wake models through lidar measurements. *Wind Energy Science*, **5**, 1601–1622, <https://doi.org/10.5194/wes-5-1601-2020>.